

# Photo-responsive Schottky Diode Behavior of a Donor-Acceptor Co-crystal with Violet Blue Light Emission

Soumen Singha,<sup>1</sup> Rajkumar Jana,<sup>1,2</sup> Rituparna Mondal,<sup>1,3</sup> Partha Pratim Ray,<sup>1</sup> Partha Pratim Bag,<sup>4</sup> Kajal Gupta,<sup>5</sup> Nandan Pakhira,<sup>5</sup> Corrado Rizzoli,<sup>6</sup> Arabinda Mallick,<sup>5</sup> Sanjay Kumar,<sup>\*,1</sup> Rajat Saha<sup>\*,1,5</sup>

<sup>1</sup>Department of Physics, Jadavpur University, Jadavpur, Kolkata-700032, WB, India

<sup>2</sup>Department of Physics, Techno India University, EM-4, Sector-V, Salt lake, Kolkata-700091, India

<sup>3</sup>Department of Electronics, Barrackpore Rastraguru Surendranath College, Barrackpore, West Bengal 700120, India

<sup>4</sup>Dumka Engineering College, Dumka, Jharkhand-814101, India

<sup>5</sup>Department of Chemistry, Kazi Nazrul University, Asansol-713340, WB, India

<sup>6</sup>Dipartimento SCVSA, Università di Parma, Parco Area delle Scienze 17/A, Parma, Italy

Sl. No	Table of Contents	Page no.
1. Experimental Section		
1.1	General: Materials and Methods.	4
1.2	Synthesis of Co-crystal $\{(C_8H_2Br_4O_4) \cdot (C_8H_6N_2)\}$ .	4
1.3	Single Crystal X-ray Diffraction Analysis: Crystallographic Data Collection and Refinement.	5
1.4	Qualitative and quantitative analysis of noncovalent interactions: Binding energy, MESP and NCI plot: Computational methodology. Hirshfeld surfaces analysis. Interaction energy calculations.	5-6
1.5	Photo-physical measurements: Photoluminescence Quantum Yield (PLQY) Calculation. Fluorescence microscopic image.	6-7
1.6	Computational methodology: Ground state structural and electronic properties with the simulation of absorption spectra.	7-8
1.7	Periodic Calculation: Band structure, DOS and optical properties calculation.	8-9
1.8	Device fabrication and measurement setups.	9
2. All Figures		
2.1	Figure S1: SEM micrographs of the co-crystal. Rhombohedral morphology of the crystals can be observed clearly.	10

2.2	Figure S2: ORTEP diagram of the co-crystal	10
2.3	Figure S3: Carboxylic groups are almost perpendicular to the phenyl ring of TBTA molecule	11
2.4	Figure S4: 1D supramolecular chain formation by O-H $\cdots$ N hydrogen bonding interactions.	11
2.5	Figure S5: Supramolecular $\pi\cdots\pi$ interactions between quinoxaline and TBTA.	11
2.6	Figure S6: Br $\cdots$ O interactions among TBTA molecules in co-crystal.	12
2.7	Figure S7: 3D supramolecular structure formed by both hydrogen bonding and $\pi\cdots$ interactions.	12
2.8	Figure S8: PXRD pattern of the co-crystal.	13
2.9	Figure S9. Thermogravimetric plot of the co-crystal.	13
2.10	Figure S10: IR spectroscopic plots of the co-crystal and one of the components TBTA measured in ATR mode.	14
2.11	Figure S11. 2D fingerprint plots of TBTA-quinoxaline showing the relative surface area of different types of interactions contributed to the total Hirshfeld surface.	14
2.12	Figure S12. Energy framework as seen along a-axis depicting electrostatic energy, dispersion energy and total energy for a cluster of molecules within 2 $\times$ 2 $\times$ 2 unit cell.	15
2.13	Figure S13. Interaction energies between pairs of constituent molecules describing O-H $\cdots$ N hydrogen bonding interactions and $\pi\cdots$ stacking interactions and their values in KJ/mol.	15
2.14	Figure S14: Interaction energies between the constituent molecules showing Br $\cdots$ O halogen bonding along with Br $\cdots\pi$ and C-H $\cdots\pi$ interactions and their values in KJ/mol.	16
2.15	Figure S15: Interaction energies between the homo-dimers showing Br $\cdots$ O halogen bonding interactions and their values in KJ/mol.	16
2.16	Figure S16: (a) Solid state UV-DRS spectra of the co-crystal and its components as obtained from the thin film of the samples on the glass surface, (b) UV-vis absorption spectra of the sample under investigation and its components in solution phase (water medium).	17
2.17	Figure S17: Concentration dependent (b) absorption spectra and (b) emission spectra of the sample in aqueous medium; (c) CIE coordinate of co-crystals according to the CIE 1931 chromaticity for solid state emission.	17
2.18	Figure S18: Ground state ( $S_0$ ) optimized geometries of the co-crystal in gas phase (a) and aqueous medium (b).	18
2.19	Figure S19: Natural transition orbitals (NTOs) for co-crystal elucidating the nature of singlet excited states in the absorption bands of gaseous state	18-19

	optimized geometry in comparison with the experimentally obtained pattern in water medium. For each state, the respective number of the state, transition energy (eV), and the oscillator strength (in parentheses) are listed.	
2.20	Figure S20: Natural transition orbitals (NTOs) for co-crystal elucidating the nature of singlet excited states in the absorption bands in comparison with the experimentally obtained pattern in water medium. For each state, the respective number of the state, transition energy (eV), and the oscillator strength (in parentheses) are listed.	19
2.21	Figure S21. Calculated band structure of co-crystal in the energy range of -6 eV to 10 eV.	20
2.22	Figure S22: Total DOS for co-crystal and the PDOS contributed from each type atoms.	21
2.23	Figure S23: Total DOS and partial density of states contributed from the two molecular fragments of the co-crystal.	21
3. All tables		
3.1	Table S1: Crystallographic data and refinement parameters of the co-crystal.	22
3.2	Table S2: Hydrogen bonding interaction parameters of the co-crystal.	22
3.3	Table S3: $\pi \cdots \pi$ interaction parameters of co-crystal.	23
3.4	Table S4: Br $\cdots$ O interaction parameters of co-crystal.	23
3.5	Table S5: Br $\cdots\pi$ interaction parameters of co-crystal.	23
3.6	Table S6: Coordinates of the ground state ( $S_0$ ) optimized geometry of co-crystal in gaseous phase.	24
3.7	Table S7: Coordinates of the ground state ( $S_0$ ) optimized geometry of co-crystal in water medium.	25
3.8	Table S8: Comparison of selected bond distances between the calculated geometries and the initial crystalline geometry for the co-crystal	26
3.9	Table S9: Selected Molecular orbitals along with their energies and compositions coming from different fragments of the co-crystal optimized in gaseous phase and water medium.	26
3.10	Table S10: Mulliken charges over the atoms of the individual components and dimer geometry at B3LYP-GD3BJ/6-311++G(d,p) level of calculation.	27
3.11	Table S11: Mulliken charges over the component fragments of the dimer geometry at B3LYP-GD3BJ/6-311++G(d,p) level of calculation.	27
3.12	Table S12: Experimental UV-Vis transitions for the co-crystal in water medium with the corresponding theoretically calculated UV-Vis transitions with vertical excitation energies ( $E_{ex}$ ), oscillator strengths ( $f$ ) of the lowest few excited singlets obtained from TDDFT/B3LYP method in gaseous state.	28-29
3.13	Table S13: Experimental UV-Vis transitions for the co-crystal in water medium with the corresponding simulated/ theoretically calculated UV-Vis transitions with vertical excitation energies ( $E_{ex}$ ), oscillator strengths ( $f$ ) of	29-30

	the lowest few excited singlets obtained from TDDFT/B3LYP/CPCM method in water. Table S12: The outcomes of the Band structure analysis of the supramolecular assembly and the corresponding inferences.	
3.14	Table S14: The outcomes of the Band structure analysis of the supramolecular assembly and the corresponding inferences.	30
4.	Hirshfeld surface analysis and Fingerprint Plots: Details of colour code used.	30-31
5.	Molecular Electrostatic Surface Potential.	31-32
6.	Change in absorption behaviour of the co-crystal from its coformers.	32
7.	Photoconductivity in the light of thermionic emission (TE) theory.	33-36
8.	Calculation of energy level of the components and the dimer geometry.	36-37
9.	References	37-40

## 1. EXPERIMENTAL SECTION

**1.1 General: Materials and Methods:** All the reagents, TBTA, quinoxaline and all the solvents were purchased from commercial sources and used without further purification. Elemental analyses (C, H, N analysis) were carried out using a Perkin Elmer 240C elemental analyzer. IR studies were done on a Nicolet Impact 410 spectrometer between 400 and 4000  $\text{cm}^{-1}$  using KBr pellet method and on Shimadzu, 8400S FT-IR spectrometer in ATR mode using pure solid samples. Powder X-ray diffraction data were collected at ambient temperature (20 °C) on a Bruker D8 Advance diffractometer operating in the reflection mode using  $\text{CuK}\alpha$  radiation having wavelength 1.5418 Å. The FESEM micrographs of the thin films prepared were recorded by an FEI INSPECT F50 field emission scanning electron microscope (FESEM).

**1.2 Synthesis of co-crystal  $\{(\text{C}_8\text{H}_2\text{Br}_4\text{O}_4)\cdot(\text{C}_8\text{H}_6\text{N}_2)\}$ :** TBTA (0.5 mmol, 0.241 g) was dissolved in 20 ml of ethanol-water mixture. The solution was stirred for 10 min. Quinoxaline (0.5 mmol, 0.066 g) was dissolved in 10 ml ethanol, and it was added slowly with the previous solution and then stirring for another 10 min. The resultant clear solution was allowed to evaporate under ambient temperature. After few days, colourless rhombohedral crystals suitable for X-ray single crystal diffraction were obtained. Yield: 72%. IR: 3432(b), 2942(w), 2855(w), 1723(s), 1648(br), 1601(vs), 1511(br), 1470(s),

1422(w), 1417(w), 1397(s), 1310(w), 1272(w), 1247(w), 1130(w), 1068(w), 811(w), 673(w), 612(w), 550(w), 515(w). Anal. Calcd. for co-crystal: C: 31.40% (31.37% theo), H: 1.30% (1.28% theo) and N: 4.60% (4.57% theo).

**1.3 Single crystal X-ray diffraction analysis: Crystallographic data collection and refinement:** Suitable single crystal was mounted on a Bruker SMART diffractometer equipped with a graphite monochromator and Mo-K $\alpha$  ( $\lambda = 0.71073 \text{ \AA}$ ) radiation. The structure was solved by using the SHELXS 97. Subsequent difference Fourier synthesis and least-squares refinement revealed the positions of the remaining non-hydrogen atoms. Non-hydrogen atoms were refined with independent anisotropic displacement parameters. Hydrogen atoms were placed in idealized positions, and their displacement parameters were fixed to be 1.2 times larger than those of the attached non-hydrogen atoms. Successful convergence was indicated by the maximum shift/error of 0.001 for the last cycle of the least-squares refinement. All calculations were carried out using SHELXL 97,<sup>1</sup> SHELXS 97,<sup>2</sup> PLATON 99,<sup>3</sup> ORTEP-3<sup>4</sup> and WinGX system Ver-1.64.<sup>5</sup> All crystallographic data for the compounds are summarized in **Table S1**. Non-covalent interactions are summarized in **Tables S2–S5**.

**1.4 Qualitative and quantitative analysis of noncovalent interactions:**

**Binding energy, MESP and NCI plot: Computational methodology:** All calculations were performed with the Gaussian 09 program<sup>6</sup> employing the DFT method using Becke's three parameter hybrid functional<sup>7</sup> and Lee–Yang–Parr's gradient corrected correlation functional<sup>8</sup> (B3LYP) along with 6-31g+(d,p) (for C, H, N and O) and LANL2DZ (ecp for Br) basis set.<sup>9</sup> To include the weak intermolecular interactions Grimme's third formulation of empirical correction for dispersion with Becke-Johnson damping (GD3BJ) was applied.<sup>10</sup> To find out the non-covalent interactions monomer and four types of molecule pair (model dimer) geometries were optimized starting from crystalline coordinates. For the two hetero-dimers full geometry and for two homo-dimers constrained geometry optimization carried out. While calculating interaction energies counterpoise<sup>11</sup> correction was employed to remove the basis set superposition error. Molecular electrostatic potential (MEP) surfaces have been calculated at the same level of theory and represented by mapping onto an electron density isosurface of value 0.001 au. Non covalent interactions have been carried out in Multiwfn package<sup>12</sup> with the help of Gaussian 09 and VMD<sup>13</sup> has been used for visualisation.

**Hirshfeld surfaces analysis:** Hirshfeld surfaces analysis and the associated two-dimensional (2D) fingerprint plots were calculated by using Crystal Explorer 17.0.<sup>14</sup> The Hirshfeld surface depicts the outline of the molecule within the crystal and 2D fingerprint plot identifies each type of intermolecular interaction and provide the relative area of the surface corresponding to each kind of interaction. Bond lengths to hydrogen atoms were set to typical values obtained from neutron diffraction data (C–H= 1.083 Å, N–H= 1.009 Å, and O–H = 0.938 Å). For each point on the Hirshfeld surface, if  $d_e$  is the distance from the point to the nearest nucleus external to the surface and  $d_i$  is the distance of the nearest nucleus internal to the surface, then the normalized contact distance ( $d_{norm}$ ) is given by

$$d_{norm} = \frac{(d_i - r_i^{vdW})}{r_i^{vdW}} + \frac{(d_e - r_e^{vdW})}{r_e^{vdW}}$$

where  $r_i^{vdW}$  and  $r_e^{vdW}$  are the van der Waals radii of the appropriate atoms internal and external to the surface, respectively. The value of  $d_{norm}$  is negative or positive depending on intermolecular contacts being shorter or longer than the Vander Waals separations. On the completion of calculation the parameter  $d_{norm}$  constructs a surface with a red–white–blue colour scheme, where bright red spots highlight shorter contacts, white areas represent contacts around the van der Waals separation, and blue regions are due to the longer contacts.

**Interaction energy calculations:** The pair wise intermolecular interaction energies within the components of the crystal estimated using CRYSTAL EXPLORER 17.0<sup>15</sup> following the procedure of Tan and Tiekink<sup>16</sup> from a single-point molecular wavefunction at CE-B3LYP/6-31G(d,p) level on a cluster of radius 6 Å around each of the components TBTA and quinoxaline. The interaction energies are consist of four energy components e.g. electrostatic (Eelec), polarization (Epol), dispersion (Edis) and exchange-repulsion (Erep) energy and can be summed up as  $E_{tot} = k_{ele}E_{elec} + k_{pol}E_{pol} + k_{dis}E_{dis} + k_{rep}E_{rep}$  where the k values are scaling factors.<sup>17-18</sup>

**1.5 Photo-physical measurements:** The UV-Vis absorption spectra of the co-crystal were recorded with the help of Perkin Elmer lambda 365 UV–vis spectrophotometer equipped with a solid state measurement attachment. Steady state emission spectra were recorded on a Horiba Fluoromax-4C fluorescence spectrophotometer. Luminescence lifetimes were recorded by time–correlated single–photon–counting (TCSPC) set up at room

temperature. For TCSPC measurement, the luminescence decay data were obtained from a Horiba Jobin-Yvon TCSPC set up and were analyzed by using IBH DAS6 software.

**Photoluminescence Quantum Yield (PLQY) Calculation:** The strength of the emission behaviour was verified by measuring the relative quantum yield of the sample. The measurement has been carried out with respect to a standard reference having the similar range of absorption and emission phenomena named quinine sulphate (QS) dissolved in 0.1 M H<sub>2</sub>SO<sub>4</sub>. The concentrations of the aqueous solutions of the sample and as well as the reference were adjusted in a way to maintain the value of absorbance within 0.02 to (0.02 + 0.0007) at the excitation wavelength ( $\lambda_{ex}$ ) = 314 nm. Then the PLQY value was estimated by integrating the area under fluorescence curves according to the equation

$$Q_S = Q_R \times \frac{I_S}{I_R} \times \frac{A_R}{A_S} \times \frac{\eta_S^2}{\eta_R^2}$$
, Where,  $Q_S$  and  $Q_R$  are the quantum yield of the sample under investigation and the standard reference,  $I_S$  and  $I_R$  represent the area under the photoluminescence curves of the sample and the reference respectively when hit at the same excitation wavelength,  $A_R$  and  $A_S$  stand for the values of absorbance or the optical densities at the excitation wavelength of the reference and the sample respectively and  $\eta_S$ ,  $\eta_R$  are the refractive indices of the solvents for the sample and the reference respectively. Here the QY of quinine sulphate ( $Q_R$ ) = 0.54 and the refractive index of pure water = 1.33 are known.

**Fluorescence microscopic image:** Fluorescence microscopic images of the co-crystal grown on a clear transparent glass slide by dropcast method were taken by Zeiss AxiocamMRc fluorescence microscope with 100x zooming. The solid state photoluminescence (PL) spectrum of the co-crystal shows a distinct emission band centred around ~ 400 nm by exciting at 257 nm. Fluorescence microscopic images of the co-crystal were collected with UV light excitation. Microscopic images clearly indicate violet–blue particles of uniform sizes.

**1.6 Computational methodology: Ground state structural and electronic properties with the simulation of absorption spectra:** The ground state ( $S_0$ ) geometries were fully optimized in gaseous phase and water medium with very tight criteria for geometry optimization at B3LYP-GD3BJ/6-311++G(d,p) level of theory using Gaussian 09 DFT package. To better reflect the solvation effect on the supramolecular complex, aqueous

cavity in solvent reaction field (SCRF) was included at conductor-like polarizable continuum (CPCM) level. Vibrational analyses were carried out by using the optimized geometries. The stationary point corresponding to one of the minima of the potential energy surface was detected by carrying out a normal mode analysis, where all vibrational frequencies were found to be positive. To compute the UV-Vis transition of the co-crystal, a single point calculation was carried out using the time dependent density functional method (TDDFT) starting with the ground state geometry optimized in both gaseous phase and water media using the same functionals and basis set. The excitation energies of the co-crystal in water medium were simulated by the conductor-like polarisable continuum model (CPCM model) using the so-called non-equilibrium approach, which has been designed for the study of the absorption process. Only singlet–singlet transitions have been considered for de-convolution of UV-Vis transitions. Orbital analysis was carried out with the help of GaussView and the MO composition analysis was done with Gausssum program.<sup>19</sup> The excited state computational results are interpreted using natural transition orbital (NTO) analysis based on the calculated transition density matrices.<sup>20-23</sup>

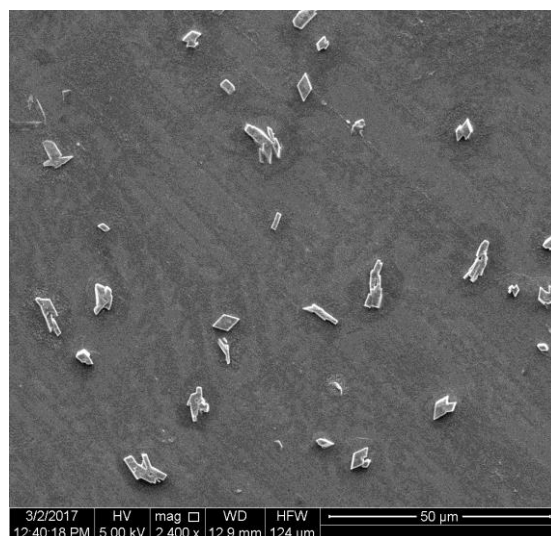
**1.7 Periodic Calculation: Band Structure and DOS Calculation:** The opto-electronic properties of the co-crystal were probed by carrying out first principal calculation with density functional theorem (DFT) utilizing the Cambridge serial total energy package (CASTEP) code.<sup>24</sup> The total energy, Band Structure (BS) and Density of States (DOS) were calculated on the geometry obtained from the single crystal X-ray diffraction data, no prior optimization of geometry or unit cell were carried out as the weak supramolecular interactions within the co-crystal get disrupted haphazardly as a result in change in orientation between the functional groups due to optimization. The exchange correlation corrected Perdew-Burke-Ernzerhof function of generalized gradient approximation (GGA/PBE)<sup>25</sup> was employed in every calculation. The ultrasoft pseudo-potential<sup>26</sup> represented in reciprocal space was used to mimic the interaction between the electrons and ionic core and the valence electrons were treated with plane wave basis set where the number of plane waves included was determined by the kinetic cut off energy ( $E_c$ ) of 630 eV for energies and subsequent properties calculations. The numerical integration over the first Brillouin zone was carried out using Monkhorst–Pack k-point sampling scheme<sup>27</sup> with a k-point mesh of  $2 \times 2 \times 1$ . The tolerance value for self-consistent field (SCF) Eigen-energy convergence was  $5 \times 10^{-7}$  eV/atom for all calculations. Pseudo-



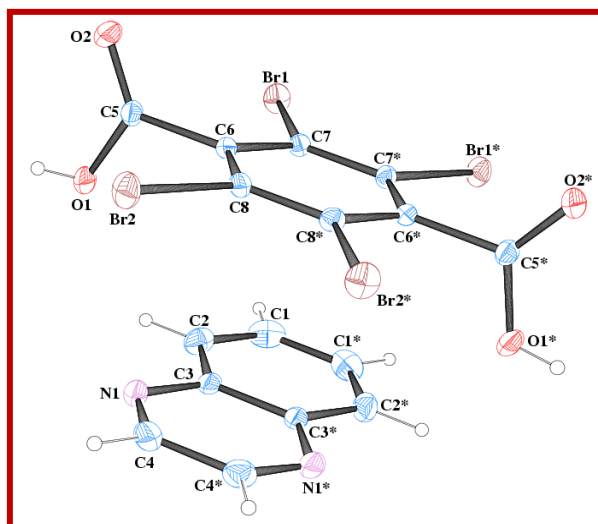
atomic calculations were performed by using H-1s<sup>1</sup>, C-2s<sup>2</sup>2p<sup>2</sup>, N-2s<sup>2</sup>2p<sup>3</sup>, O-2s<sup>2</sup>2p<sup>4</sup> and Br-4s<sup>2</sup>4p<sup>5</sup> valence electron configurations for the constituent atoms. Moreover, the long-range dispersion correction was incorporated by Grimme's DFT-D method.<sup>28</sup>

**Optical properties calculations:** The prime aspect of the optical properties of any material is its dielectric function as it can describe optical response of the medium at all photon energies of the e. m. radiation due to the interaction the photons with electrons. Its imaginary part  $\epsilon''(\omega)$  can directly be derived from the electronic band structure of a material by applying suitable scissor operator value considering the interband optical transitions by estimating the dipole moment matrix elements between the occupied and unoccupied states (wave functions) within the selection rule. The real part  $\epsilon'(\omega)$  of the dielectric function can be derived from  $\epsilon''(\omega)$  by using the Kramers–Kronig relationship. All other important frequency dependent optical properties such as refractive index  $n(\omega)$ , extinction coefficient  $k(\omega)$ , absorption coefficient  $\alpha(\omega)$ , optical conductivity  $\sigma(\omega)$ , reflectivity  $R(\omega)$  and electron energy-loss function  $L(\omega)$  can be extracted from the knowledge of both  $\epsilon'(\omega)$  and  $\epsilon''(\omega)$ .<sup>29-30</sup>

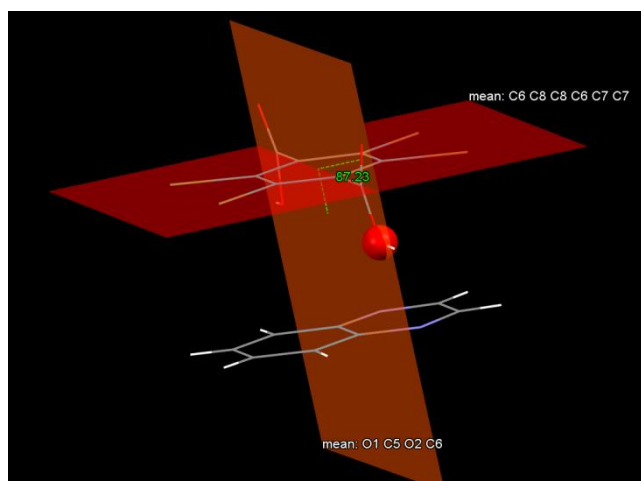
**1.8 Device fabrication and measurement setups:** To measure the electrical conductivity and photo responsivity, schottky barrier diodes (SBD) are fabricated with Al/synthesized material/ITO sandwiched configuration. Here, the indium tin oxide (ITO) coated glass substrates are cleaned using isopropanol, acetone and deionized water sequentially with the help of an ultrasonication system and then placed into a vacuum chamber for drying. Then, the synthesized materials are dispersed in chloroform medium. To develop an active thin film, the solution of the materials are spun upon the cleaned ITO with the help of an SCU 2700 spin coating system at 2000 rpm for 2 min followed by drying in a desiccator for overnight and characterized by PXRD analysis. The thickness of the deposited films are measured as  $\sim 1.0 \mu\text{m}$ . Aluminum (Al) electrode is deposited on the active thin film by a Vacuum Coating Unit 12A4D of HINDHIVAC using shadow mask. The distance between the two Al probes are maintained at  $5 \mu\text{m}$ . The effective area (A) of the SBD is measured as  $7.065 \times 10^{-6} \text{ m}^2$ . Now the electrical conductivity of the co-crystal was carried out by two probe method using a Keithley 2635B sourcemeter interfaced with a PC by applying bias voltage from +2 to -2 V. The experiment has been carried in a dark box. The photo response measurements have been carried out under AM1.5G photo-irradiation ( $100 \text{ mW/cm}^2$ ).



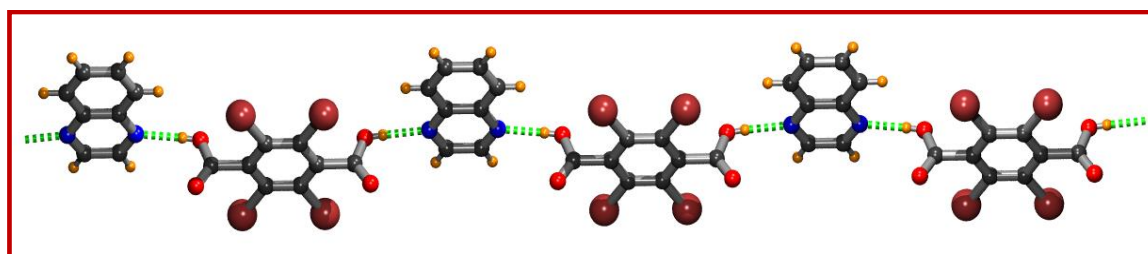
**Figure S1:** SEM micrographs of the co-crystal. Rhombohedral morphology of the crystals can be observed clearly.



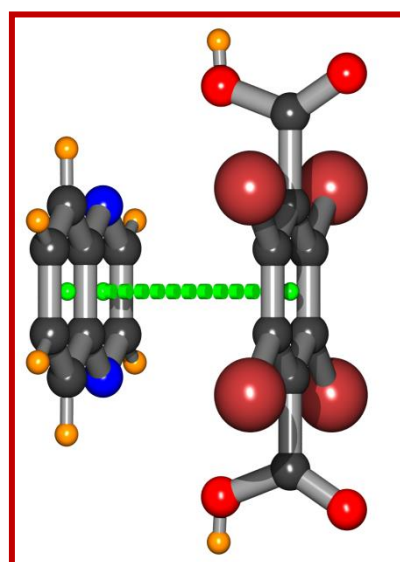
**Figure S2:**ORTEP diagram of the co-crystal



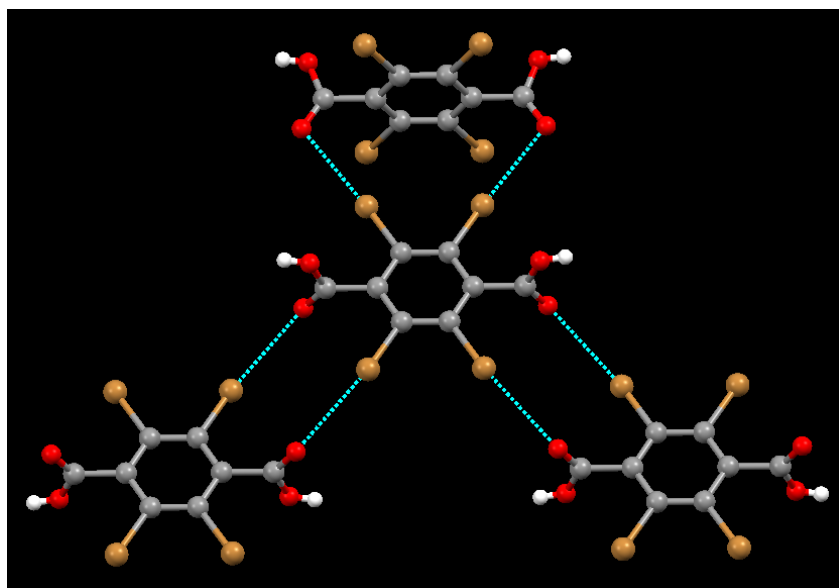
**Figure S3:** Carboxylic groups are almost perpendicular to the phenyl ring of TBTA molecule



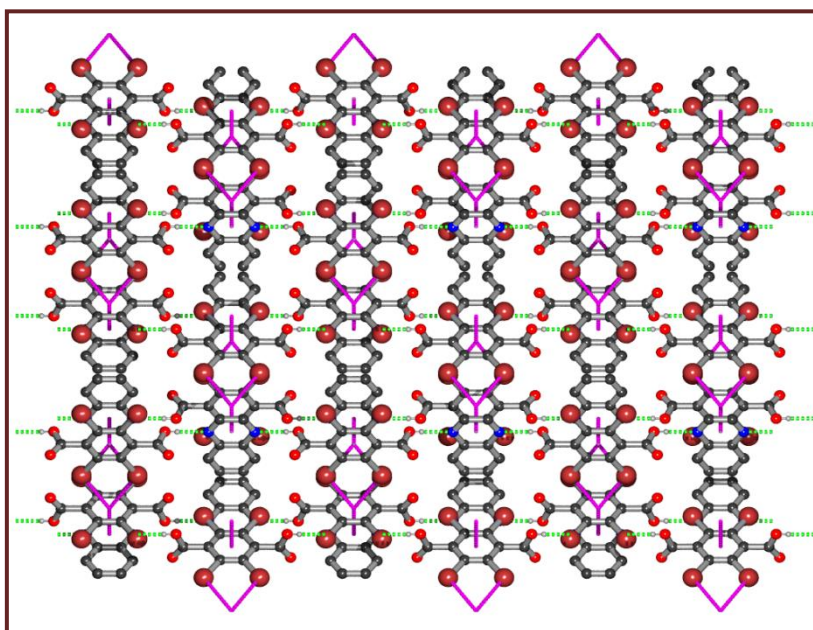
**Figure S4:** 1D supramolecular chain formation by O-H...N hydrogen bonding interactions.



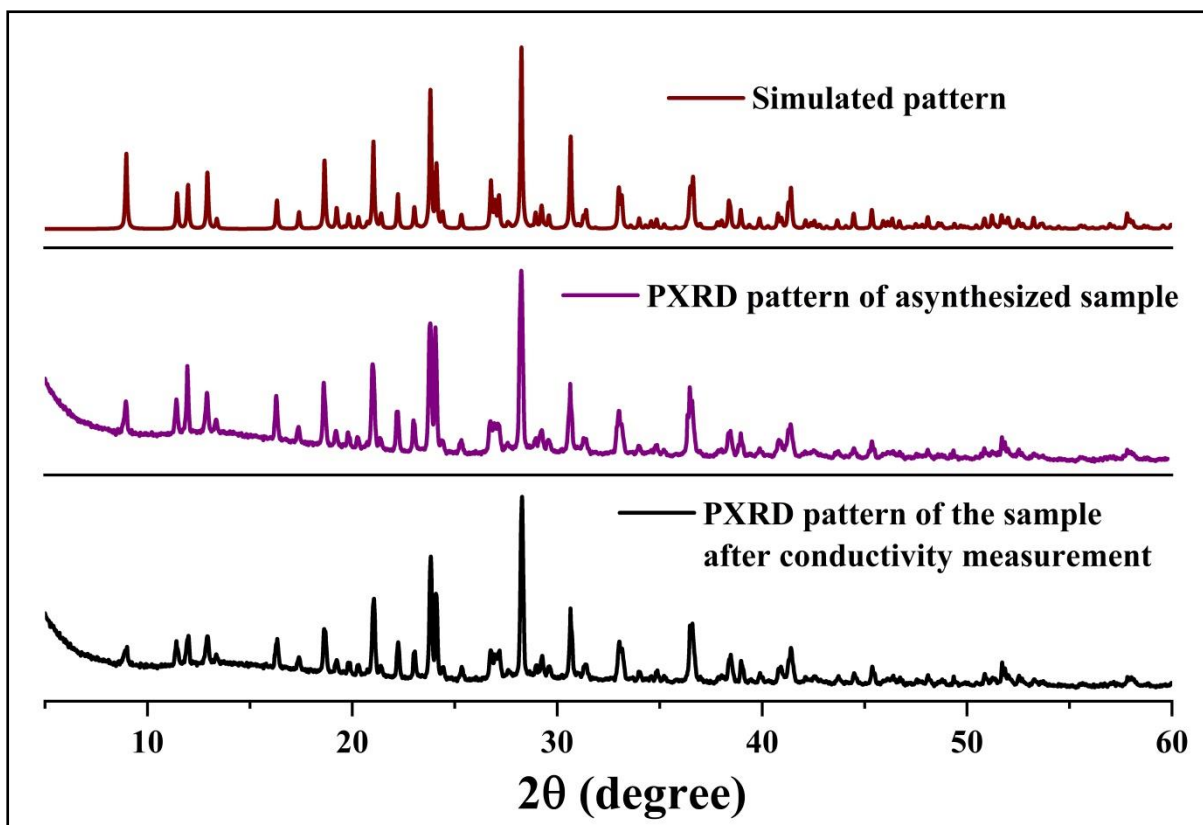
**Figure S5:** Supramolecular  $\pi \cdots \pi$  interactions between quinoxaline and TBTA.



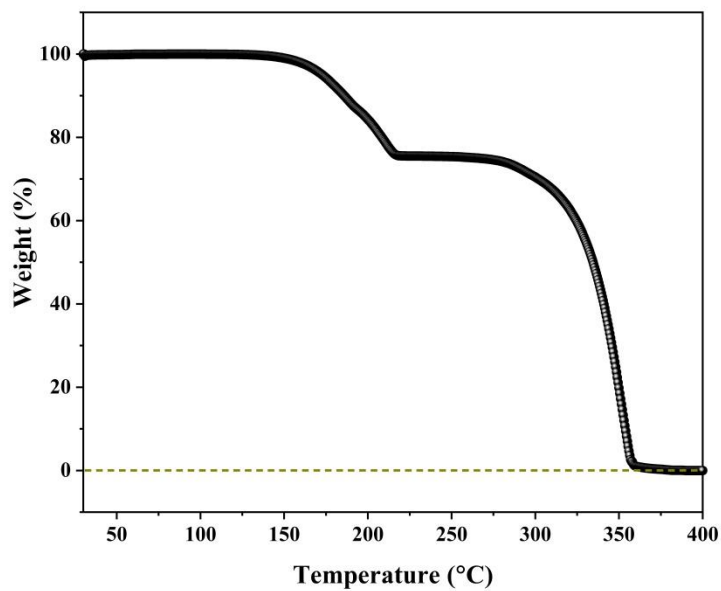
**Figure S6:** Br...O interactions among TBTA molecules in co-crystal



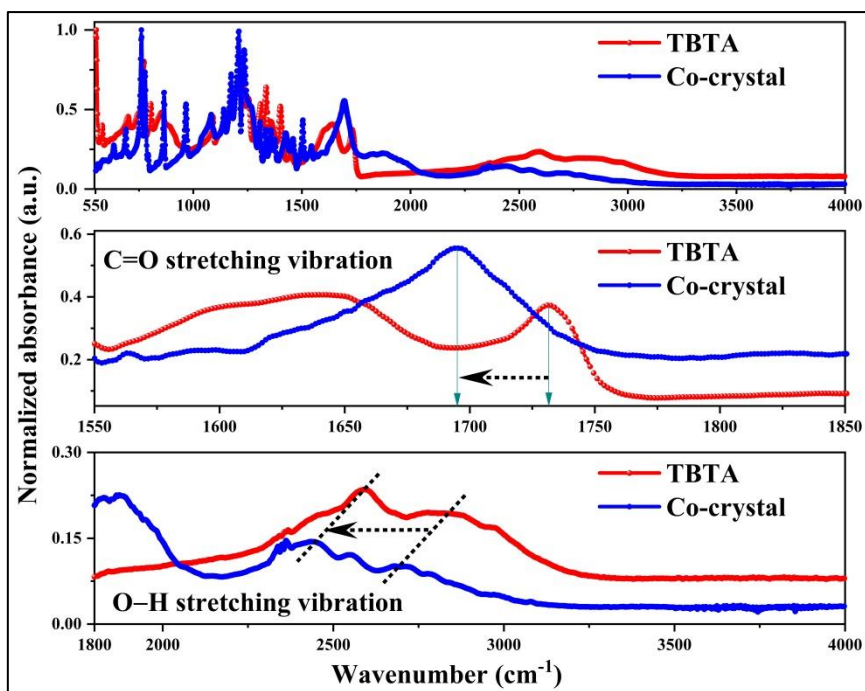
**Figure S7:** 3D supramolecular structure formed by both hydrogen bonding and  $\pi\cdots\pi$  interactions.



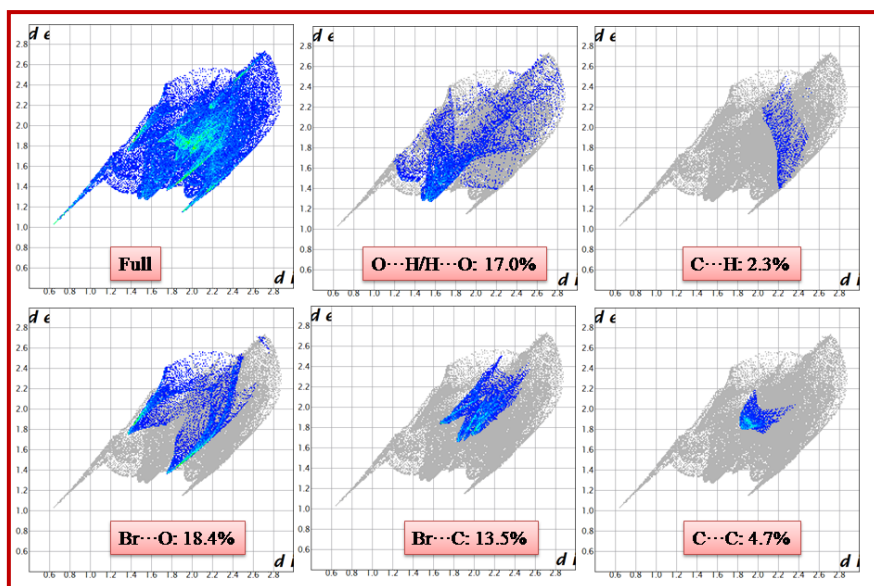
**Figure S8:** PXRD pattern of the co-crystal



**Figure S9:** Thermogravimetric plot of the co-crystal.

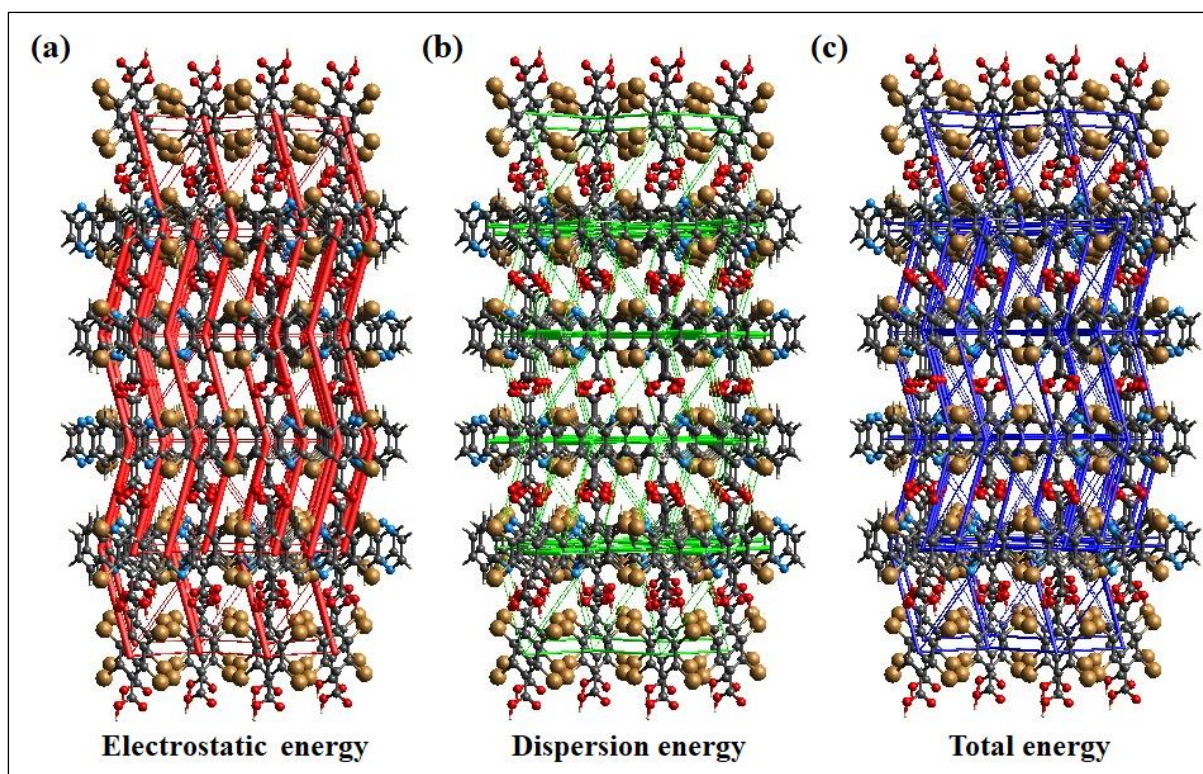


**Figure S10:** IR spectroscopic plots of the co-crystal and one of the components TBTA measured in ATR mode.

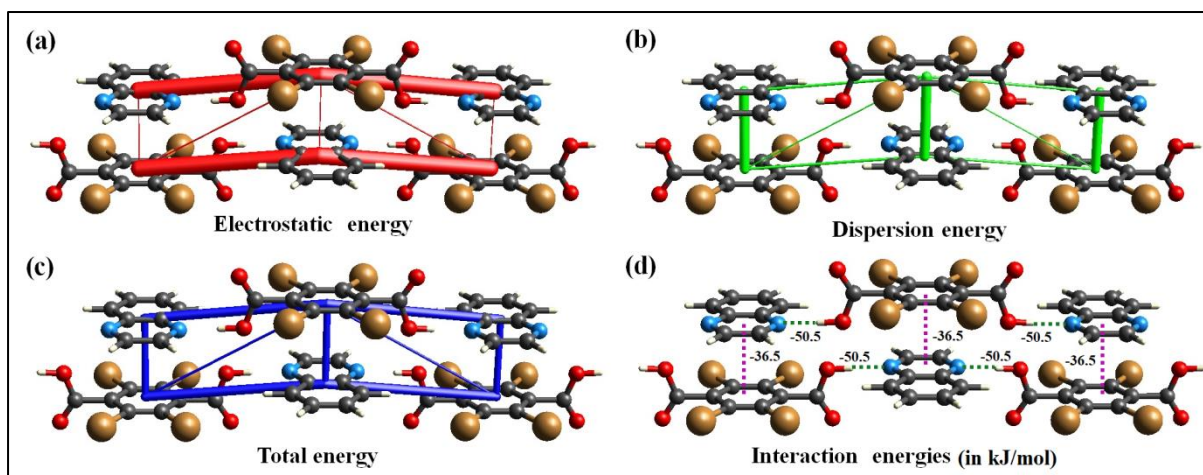


**Figure S11:** 2D fingerprint plots of TBTA-quinoxaline showing the relative surface area of different types of interactions contributed to the total Hirshfeld surface.

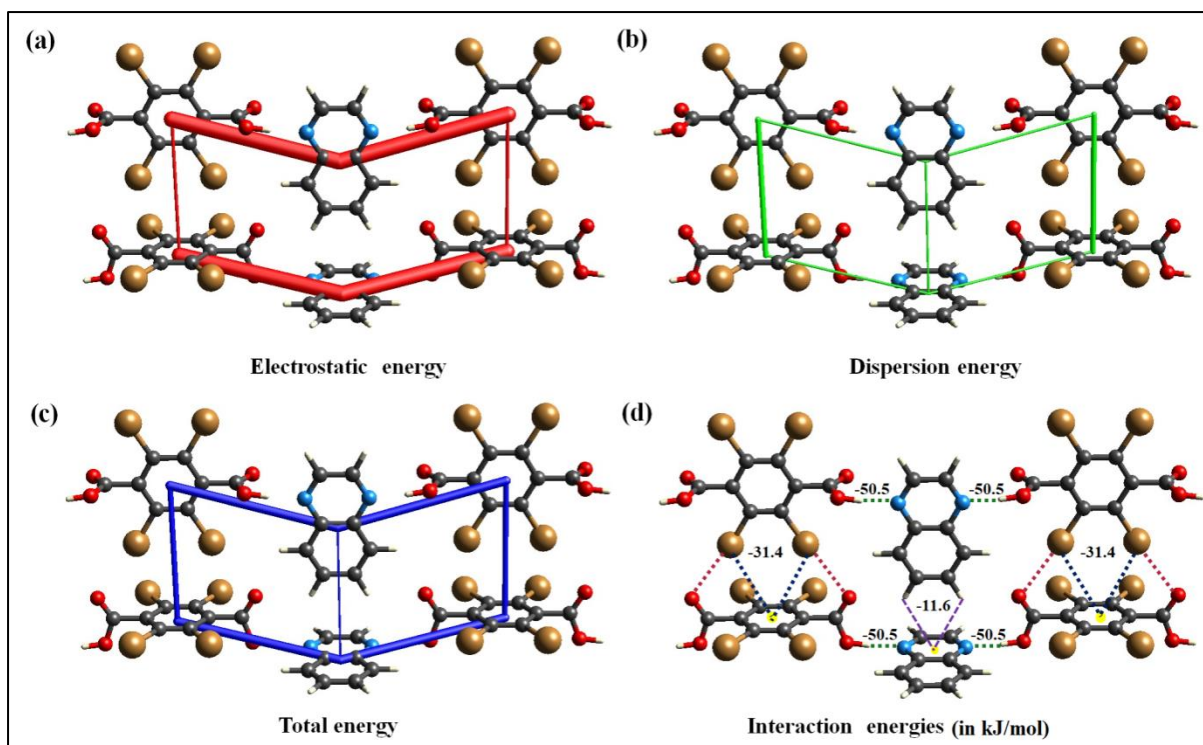




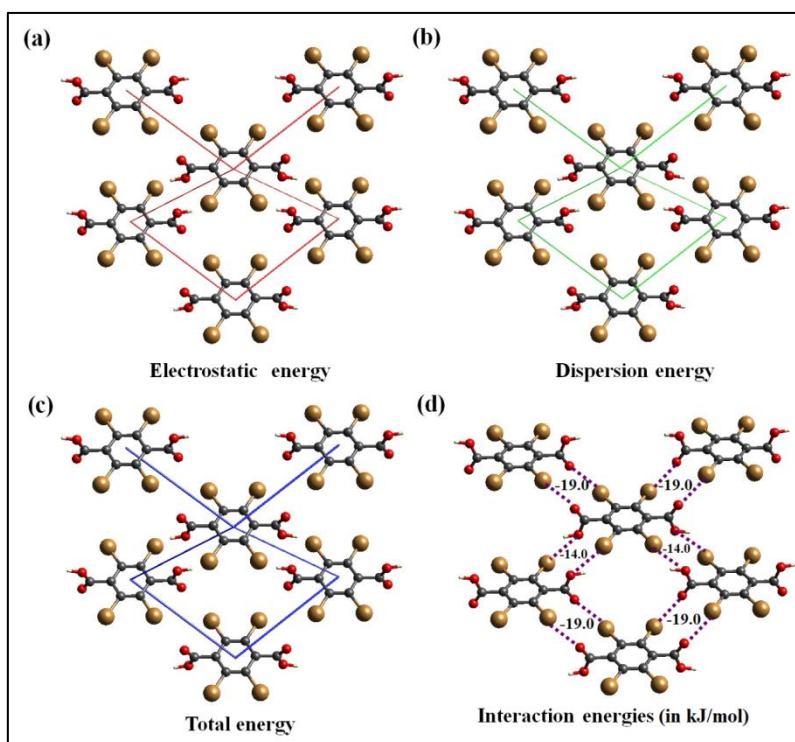
**Figure S12.** Energy framework as seen along a-axis depicting electrostatic energy, dispersion energy and total energy for a cluster of molecules within  $2 \times 2 \times 2$  unit cell and represented as cylinders joining the centroids of the interacting molecular pairs, with the radius of the corresponding cylinders proportional to the magnitude of interaction energy and colour-coded as red, green and blue for  $E_{el}$ ,  $E_{dis}$  and  $E_{tot}$  respectively with the scale factor 40 and a cut-off energy value of 10 kJ/mol.



**Figure S13.** Interaction energies between pairs of constituent molecules describing O-H $\cdots$ N hydrogen bonding interactions and  $\pi \cdots$  stacking interactions and their values in KJ/mol.

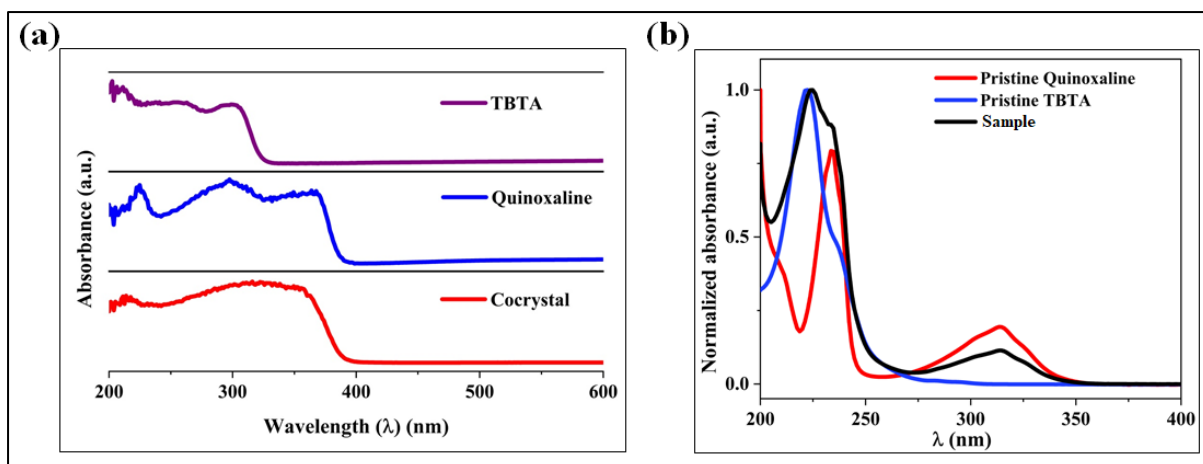


**Figure S14.** Interaction energies between the constituent molecules showing Br $\cdots$ O halogen bonding along with Br $\cdots$  $\pi$  and C–H $\cdots$  $\pi$  interactions and their values in KJ/mol.

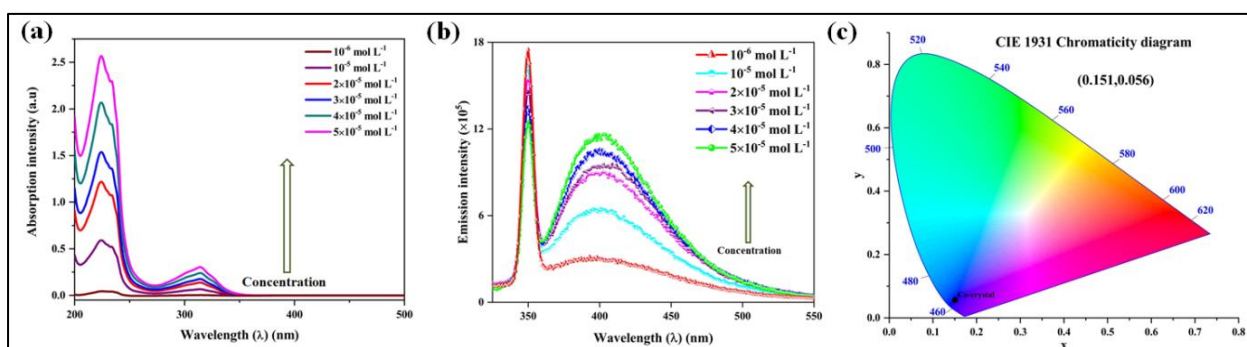


**Figure S15.** Interaction energies between the homo-dimers showing Br $\cdots$ O halogen bonding interactions and their values in KJ/mol.

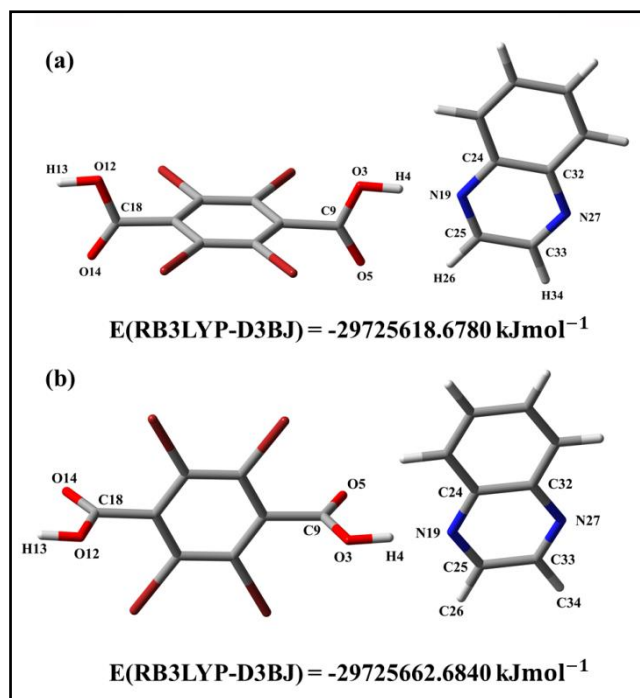




**Figure S16:** (a) Solid state UV-DRS spectra of the co-crystal and its components as obtained from the thin film of the samples on the glass surface, (b) UV-vis absorption spectra of the sample under investigation and its components in solution phase (water medium).



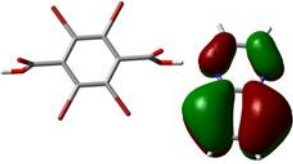
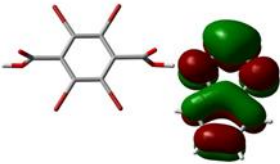
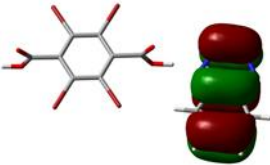
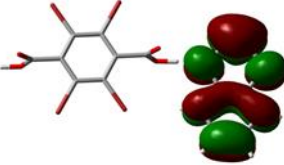
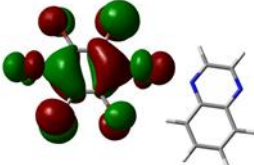
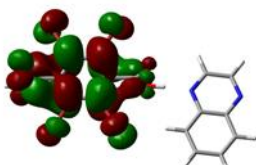
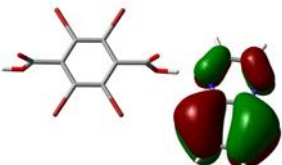
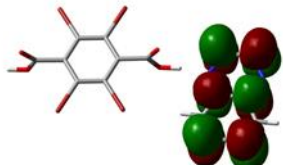
**Figure S17:** Concentration dependent (a) absorption spectra and (b) emission spectra of the sample in aqueous medium; (c) CIE coordinate of co-crystals according to the CIE 1931 chromaticity for solid state emission.



**Figure S18:** Ground state ( $S_0$ ) optimized geometries of the co-crystal in gas phase (a) and aqueous medium (b).

		Hole NTO	Particle NTO	Weight, $\lambda_i$
315 nm	$S_3$ 4.02 (0.0349) 308.49  ILCT			0.98218
294 nm	$S_6$ 4.39 (0.0861) 282.18  ILCT			0.76056
237 nm	$S_{20}$ 5.33 (0.2717) 232.75  LLCT/ILCT			0.51841
225 nm	$S_{40}$ 5.67 (0.2295) 218.82  LLCT/ILCT			0.57649

**Figure S19:** Natural transition orbitals (NTOs) for co-crystal elucidating the nature of singlet excited states in the absorption bands of gaseous state optimized geometry in comparison with the experimentally obtained pattern in water medium. For each state, the respective number of the state, transition energy (eV), and the oscillator strength (in parentheses) are listed.

		Hole NTO	Particle NTO	Weight, $\lambda_i$
315 nm	$S_2$ 3.91 (0.0464) 317.32 ILCT			0.98678
294 nm	$S_4$ 4.32 (0.1273) 287.01 ILCT			0.81189
237 nm	$S_{20}$ 5.32 (0.2977) 233.10 ILCT			0.64696
225 nm	$S_{36}$ 5.53 (0.6642) 224.17 ILCT			0.55969

**Figure S20:** Natural transition orbitals (NTOs) for co-crystal elucidating the nature of singlet excited states in the absorption bands in comparison with the experimentally obtained pattern in water medium. For each state, the respective number of the state, transition energy (eV), and the oscillator strength (in parentheses) are listed.

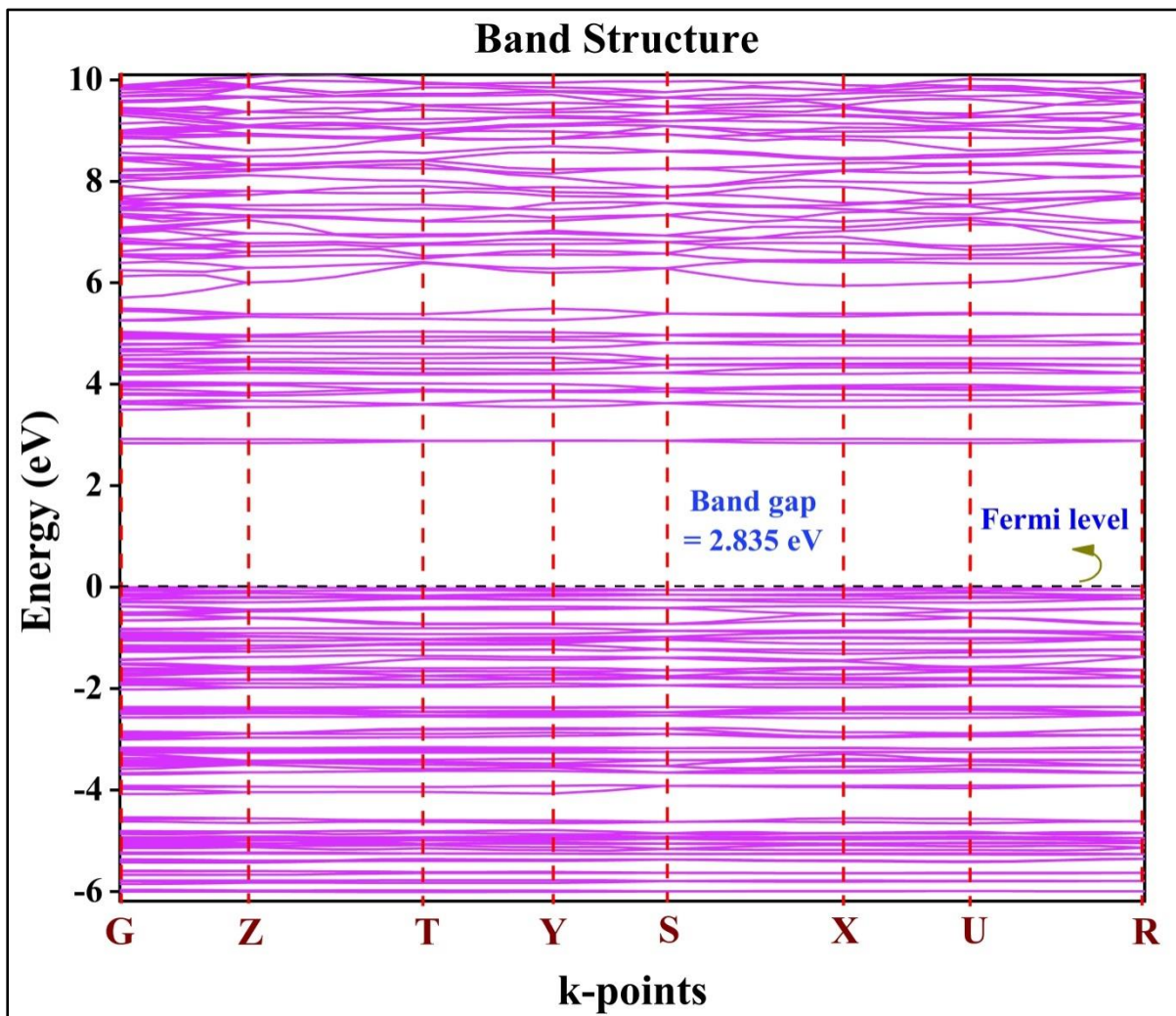
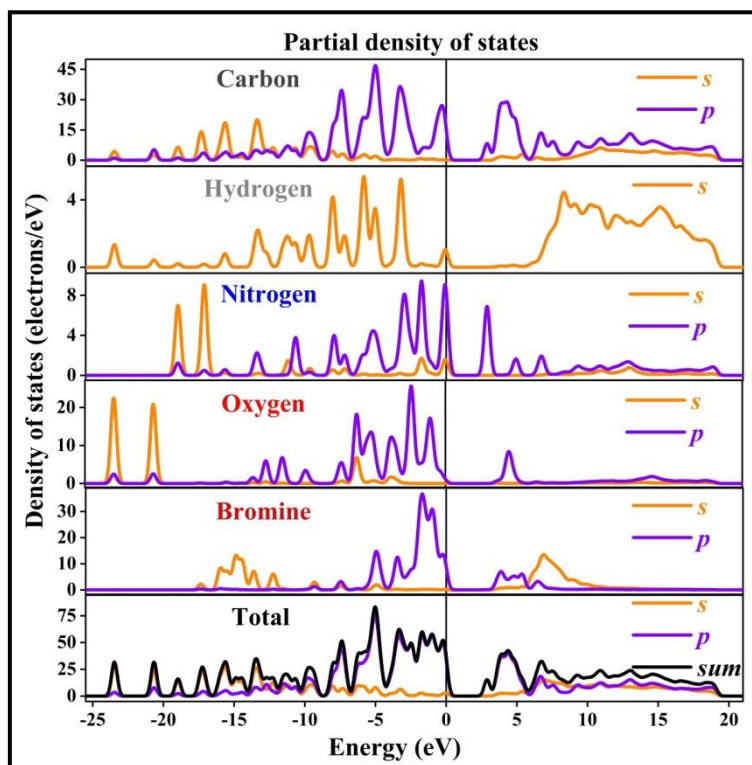
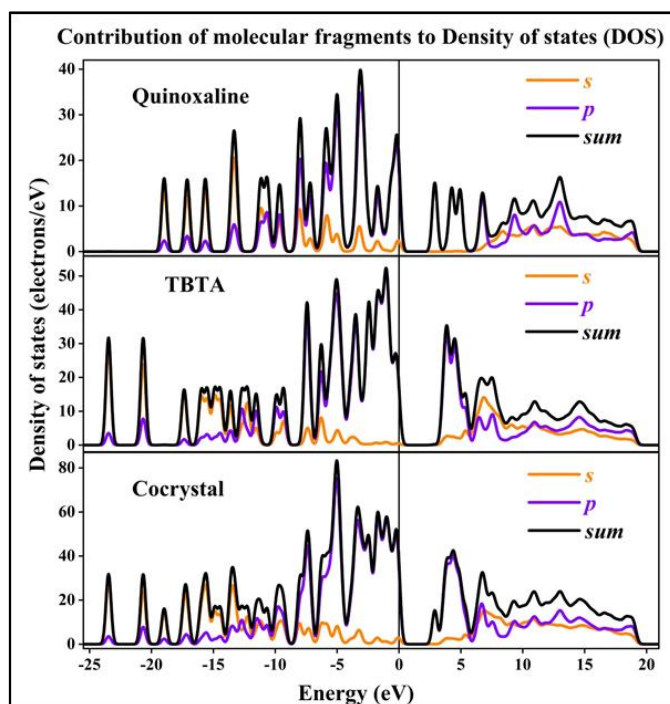


Figure S21. Calculated band structure of co-crystal in the energy range of -6 eV to 10 eV.



**Figure S22:** Total DOS for co-crystal and the PDOS contributed from each type atoms.



**Figure S23:** TDOS and PDOS contributed from the two molecular fragments of the co-crystal

**Table S1:** Crystallographic data and refinement parameters of the co-crystal.

Formula	C <sub>8</sub> H <sub>2</sub> Br <sub>4</sub> O <sub>4</sub> , C <sub>8</sub> H <sub>6</sub> N <sub>2</sub>
Formula weight	611.88
Crystal system	Orthorhombic
Space group	<i>P</i> <sub>nma</sub>
a (Å)	9.4972(18)
b (Å)	14.745(3)
c (Å)	13.181(2)
α (°)	90
β (°)	90
γ (°)	90
V(Å <sup>3</sup> )	1845.8(6)
Z	4
ρ <sub>calc</sub> (g/cm <sup>3</sup> )	2.202
μ (Mo Kα) (mm)	8.746
F(000)	1160
Crystal size (mm <sup>3</sup> )	0.16 x 0.26 x 0.28
T (K)	293
θ <sub>min-max</sub> (°)	2.1 - 27.5
Total data	29997
Unique Data	2199
R <sub>int</sub>	0.064
Observed data [I > 2.0σ(I)]	1576
N <sub>ref</sub>	2199
N <sub>par</sub>	119
R	0.0278
wR <sub>2</sub>	0.0624
S	1.02

$$w = 1/[\sigma^2(F_o^2) + (0.0827P)^2 + 4.5781P] \text{ where } P = (F_o^2 + 2F_c^2)/3$$

**Table S2:** Hydrogen bonding interaction parameters of the co-crystal.

D–H···A	d[D–H]/(Å)	d[H···A]/(Å)	d[D···A]/(Å)	∠D–H···A(°)	Symmetry
O1–H1O1···N1	0.74	1.90	2.642(3)	177	x, y, z

**Table S3:**  $\pi \cdots \pi$  interaction parameters of co-crystal.

<b>Ri···Rj</b>	<b>sym. Equivalence</b>	<b><math>d[\text{Ri} \cdots \text{Rj}]</math> (Å)</b>	<b><math>\alpha</math> (°)</b>	<b><math>d(\text{Ri} \cdots \perp \text{R}^j)</math> (Å)</b>
R1···R2	1-x, 1/2+y, 1-z	3.7757(18)	0.84(14)	3.5958(11)
R1···R2	1-x, 1-y, 1-z	3.7757(18)	0.84(14)	3.5958(11)
R1···R3	1-x, 1/2+y, 1-z	3.7705(19)	0.02(14)	3.5913(11)
R1···R3	1-x, 1-y, 1-z	3.7705(19)	0.02(14)	3.5913(11)
R2···R1	1-x, -1/2+y, 1-z	3.7758(18)	0.84(14)	3.5785(12)
R2···R1	1-x, 1-y, 1-z	3.7758(18)	0.84(14)	3.5785(12)
R3···R1	1-x, -1/2+y, 1-z	3.7706(19)	0.02(14)	3.5920(14)
R3···R1	1-x, 1-y, 1-z	3.7706(19)	0.02(14)	3.5920(14)

**Table S4:** Br···O interaction parameters of co-crystal.

<b>C-Br···O</b>	<b>sym. Equivalence</b>	<b><math>\angle \text{C-Br} \cdots \text{O}</math> (°)</b>	<b><math>d(\text{Br} \cdots \text{O})</math> (Å)</b>	<b>Sum of vdW radii of Br and O (Å)</b>	<b>Change in Br···O distance due to halogen interaction (Å)</b>
C7-Br1···O2*	-x, 1-y, 1-z	164.68	3.264(2)	3.35	0.09
C8-Br2···O2*	1/2+x, y, 1/2-z	171.37	3.124(2)	3.35	0.23

**Table S5:** Br··· $\pi$  interaction parameters of co-crystal.

<b>Y-Br···Cg</b>	<b><math>d[\text{Br} \cdots \text{Cg}]</math> (Å)</b>	<b><math>d[\text{Br} \cdots \perp \text{Cg}^i]</math> (Å)</b>	<b><math>\angle \text{Y-Br} \cdots \text{Cg}</math> (°)</b>	<b>sym. equivalence</b>
C3-Br2···R1	3.8770(14)	3.464	122.07(8)	1/2+x, 1/2-y, 3/2-z
C3-Br2···R1	3.8770(14)	3.464	122.07(8)	1/2+x, y, 3/2-z

**R1:** Cg1: C(1)-> C(2)-> C(3)-> C(3)a-> C(2)a-> C(1)a->; **R2:** Cg2: N(1)-> C(7)-> C(7)b-> N(1)b-> C(8)b-> C(8)->; **Cg3:** C(5)-> C(6)-> C(7)-> C(7)b-> C(6)b-> C(5)b->;



**Table S6:** Coordinates of the ground state ( $S_0$ ) optimized geometry of co-crystal in gaseous phase.

Tag	Symbol	X	Y	Z
1	Br	-0.2016	-2.8348	-0.4143
2	Br	-0.2016	2.8348	-0.4143
3	O	1.7445	0.0000	0.3610
4	H	2.7260	0.0000	0.0916
5	O	1.3733	0.0000	-1.8629
6	C	-1.1738	-1.2086	-0.2324
7	C	-0.4896	0.0000	-0.3750
8	C	-1.1738	1.2086	-0.2324
9	C	0.9852	0.0000	-0.7171
10	Br	-3.5151	-2.8340	0.2462
11	Br	-3.5151	2.8340	0.2462
12	O	-4.9991	0.0000	1.7303
13	H	-5.9648	0.0000	1.8237
14	O	-5.5450	0.0000	-0.4564
15	C	-2.5449	-1.2096	0.0410
16	C	-3.2304	0.0000	0.1708
17	C	-2.5449	1.2096	0.0410
18	C	-4.7191	0.0000	0.4142
19	N	4.3197	0.0000	-0.3781
20	C	6.2531	0.0000	2.7216
21	H	6.0973	0.0000	3.7938
22	C	5.1718	0.0000	1.8741
23	H	4.1553	0.0000	2.2486
24	C	5.3820	0.0000	0.4757
25	C	4.5631	0.0000	-1.6704
26	H	3.7003	0.0000	-2.3289
27	N	6.9422	0.0000	-1.3847
28	C	7.5746	0.0000	2.2116
29	H	8.4096	0.0000	2.9019
30	C	7.8040	0.0000	0.8574
31	H	8.8042	0.0000	0.4426
32	C	6.7117	0.0000	-0.0430
33	C	5.8905	0.0000	-2.1702
34	H	6.0634	0.0000	-3.2421



**Table S7:** Coordinates of the ground state ( $S_0$ ) optimized geometry of co-crystal in water medium.

Tag	Symbol	X	Y	Z
1	Br	-0.8575	-3.1326	-0.1899
2	Br	0.5576	2.3559	-0.3682
3	O	1.6696	-0.8044	0.6635
4	H	2.6754	-0.9856	0.5108
5	O	1.4803	-0.8476	-1.5832
6	C	-1.4053	-1.3093	-0.1371
7	C	-0.4331	-0.3155	-0.2611
8	C	-0.8021	1.0302	-0.2116
9	C	1.0198	-0.6910	-0.4726
10	Br	-4.1064	-2.2810	0.2056
11	Br	-2.6916	3.2055	0.0242
12	O	-4.9313	0.9015	1.4726
13	H	-5.8719	1.1439	1.5136
14	O	-5.3053	0.9249	-0.7502
15	C	-2.7484	-0.9586	0.0266
16	C	-3.1169	0.3877	0.0640
17	C	-2.1445	1.3834	-0.0497
18	C	-4.5723	0.7670	0.1926
19	N	4.2618	-1.1660	0.3687
20	C	5.3780	2.3146	0.4205
21	H	4.9701	3.3125	0.5245
22	C	4.5401	1.2263	0.4660
23	H	3.4730	1.3429	0.6055
24	C	5.0786	-0.0741	0.3288
25	C	4.8068	-2.3544	0.2343
26	H	4.1515	-3.2176	0.2633
27	N	7.0263	-1.4888	0.0107
28	C	6.7732	2.1491	0.2391
29	H	7.4113	3.0236	0.2075
30	C	7.3195	0.8955	0.1045
31	H	8.3833	0.7488	-0.0345
32	C	6.484	-0.2463	0.1455
33	C	6.2039	-2.5122	0.0552
34	H	6.6232	-3.5069	-0.0509

**Table S8:** Comparison of selected bond distances between the calculated geometries and the initial crystalline geometry for the **co-crystal**

Bond	Bond distances (Å)		
	Gas phase	Water medium	Crystalline geometry (Experimental)
C9-O5	1.210	1.212	1.192
C9-O3	1.319	1.314	1.302
O3-H4	1.018	1.033	0.743
C18-O14	1.200	1.205	1.192
C18-O12	1.346	1.336	1.302
O12-H13	0.970	0.972	0.743
C24-N19	1.363	1.364	1.363
N19-C25	1.315	1.314	1.300
C32-N27	1.361	1.362	1.363
N27-C33	1.313	1.314	1.300
C25-H26	1.085	1.084	0.930
C33-H34	1.086	1.085	0.930

**Table S9:** Selected Molecular orbitals along with their energies and compositions coming from different fragments of the co-crystal optimized in gaseous phase and water medium.

MO	Energy (eV)		%Composition			
	Gas	Water	Gas		Water	
			TBTA	QUIN	TBTA	QUIN
LUMO + 4	-1.54	-1.36	0	100	1	99
LUMO + 3	-1.64	-1.78	100	0	100	0
LUMO + 2	-1.69	-1.84	100	0	100	0
LUMO + 1	-1.85	-1.96	100	0	100	0
LUMO	-2.88	-2.75	0	100	0	100
HOMO	-7.08	-7.24	100	0	100	0
HOMO – 1	-7.38	-7.30	96	4	0	100
HOMO – 2	-7.50	-7.55	0	100	93	7
HOMO – 3	-7.76	-7.67	7	93	10	90
HOMO – 4	-7.87	-7.68	0	100	4	96

**HOMO – LUMO energy gap:** 4.20 eV (in gas phase)  
4.49 eV (in water medium)

**Table S10:** Mulliken charges over the atoms of the individual components and dimer geometry at B3LYP-GD3BJ/6-311++G(d,p) level of calculation.

Sl. No.	Atom	Charges on component geometries	Charges on H-bonded dimer	Changes due to dimerization
1	Br	-0.09645	-0.1383	-0.04185
2	Br	-0.09645	-0.1383	-0.04185
3	O	-0.02264	-0.09478	-0.07214
4	H	0.28082	0.89312	0.6123
5	O	-0.12447	-0.09271	0.03176
6	C	-0.11424	-0.06204	0.05221
7	C	0.67248	0.30016	-0.37233
8	C	-0.24951	-0.06208	0.18743
9	C	-0.24954	-0.9488	-0.69926
10	Br	-0.09645	-0.10876	-0.01231
11	Br	-0.09645	-0.10876	-0.01231
12	O	-0.02264	-0.01408	0.00857
13	H	0.28082	0.28199	0.00117
14	O	-0.12447	-0.11917	0.0053
15	C	-0.11424	0.04071	0.15495
16	C	0.67248	0.61782	-0.05467
17	C	-0.24951	0.04063	0.29014
18	C	-0.24954	-0.1083	0.14124
19	N	-0.01923	-0.13688	-0.11765
20	C	-0.21204	-0.41143	-0.19939
21	H	0.17213	0.19017	0.01804
22	C	-0.20475	0.00872	0.21348
23	H	0.19405	0.15306	-0.04099
24	C	-0.14408	-0.05105	0.09303
25	C	0.0129	0.32501	0.31211
26	H	0.20102	0.25928	0.05826
27	N	-0.01923	-0.00796	0.01127
28	C	-0.21204	-0.25549	-0.04346
29	H	0.17213	0.17527	0.00314
30	C	-0.20475	-0.17284	0.03192
31	H	0.19405	0.2077	0.01365
32	C	-0.14408	-0.35036	-0.20628
33	C	0.0129	-0.3319	-0.3448
34	H	0.20102	0.22035	0.01933

**Table S11:** Mulliken charges over the component fragments of the dimer geometry at B3LYP-GD3BJ/6-311++G(d,p) level of calculation.

Coformer	Charge
TBTA	0.17835 a.u.
QUIN	-0.17835 a.u.

**Table S12:** Experimental UV-Vis transitions for the co-crystal in water medium with the corresponding theoretically calculated UV-Vis transitions with vertical excitation energies ( $E_{ex}$ ), oscillator strengths ( $f$ ) of the lowest few excited singlets obtained from TDDFT/B3LYP method in gaseous state

Experimental excitation values (nm)	Calculated excitation values (nm)	Excitation energy (eV)	CI expansion coefficient	Excited state involved	Osc. strength ( $f$ )	Key transition involved
225.25	217.7491	5.6939 eV	0.35586 -0.32898 0.20278 -0.19074 0.18641	$S_{43}$	0.1908	H-3→L+2 (25%) H-2→L+4 (22%) H-12→LUMO (8%) H-8→L+1 (7%) H-4→L+7 (7%)
	218.8175	5.6661 eV	0.46593 0.34303 0.19501 0.19183 -0.17634	$S_{40}$	0.2295	H-3→L+2 (43%) H-2→L+4 (24%) H-6→L+2 (8%) H-4→LUMO (7%) H-4→L+7 (6%)
	228.7151	5.4209 eV	0.46280 -0.33705 -0.20746 0.19203	$S_{27}$	0.0527	H-5→L+2 (43%) H-1→L+6 (23%) H-1→L+3 (9%) H-1→L+4 (7%)
236.92	230.7670	5.3727 eV	0.38848 0.44842 -0.24249	$S_{24}$	0.1916	H-1→L+3 (30%) H-1→L+5 (40%) HOMO→L+2 (12%)
	232.7554	5.3268 eV	-0.30155 0.46730 0.30186	$S_{20}$	0.2717	H-10→LUMO (18%) H-1→L+2

			-0.17148			(44%) HOMO→L+3 (18%) H-6→L+2 (6%)
294.42	282.1798	4.3938 eV	0.61539 -0.33979	$S_6$	0.0861	H-4→LUMO (76%) H-2→L+4 (23%)
314.91	308.4951	4.0190 eV	0.69171	$S_3$	0.0349	H-2→LUMO (96%)

**Table S13:** Experimental UV-Vis transitions for the co-crystal in water medium with the corresponding simulated/ theoretically calculated UV-Vis transitions with vertical excitation energies ( $E_{ex}$ ), oscillator strengths ( $f$ ) of the lowest few excited singlets obtained from TDDFT/B3LYP/CPCM method in water.

Experimental excitation values (nm)	Calculated excitation values (nm)	Excitation energy (eV)	CI expansion coefficient	Excited state involved	Osc. strength (f)	Key transition involved
225.25	224.1745	5.5307 eV	0.52390 -0.20956 0.21590 -0.16976	$S_{36}$	0.6642	H-1→L+4 (55%) H-4→LUMO (9%) H-4→L+3 (9%) H-3→L+3 (6%)
	230.4881	5.3792 eV	0.28111 0.36104 0.46833	$S_{25}$	0.1308	H-4→L+2 (16%) H-2→L+2 (26%) H-3→L+2 (44%)
236.92	231.9846	5.3445 eV	-0.27335 0.40189 -0.23842	$S_{22}$	0.2604	H-3→L+2 (15%) H-2→L+2 (32%) HOMO→L+3 (11%)
	233.1011	5.3189 eV	0.43522 0.21181 0.27287	$S_{20}$	0.2977	H-2→L+3 (38%) H-2→L+5 (9%) HOMO→L+2 (15%)
	248.8692	4.9819 eV	-0.05535 0.61428	$S_{11}$	0.1308	H-2→L+2 (20%) HOMO→L+3 (75%)
294.42	287.0070	4.3199 eV	0.53443 -0.34492	$S_4$	0.1273	H-4→LUMO (57%)

			0.29890			H-3→LUMO (24%) H-1→L+4 (18%)
314.91	317.3223	3.9072 eV	0.69449	$S_2$	0.0464	H-1→LUMO (96%)

**Table S14.** The outcomes of the Band structure analysis of the supramolecular assembly and the corresponding inferences.

	<b>Cocrystal-I</b>
<b>High symmetry points of 1<sup>st</sup> Brillouin zone (k-points)</b>	G(0.000,0.000,0.000), Z(0.000,0.000,0.500), T(-0.500,0.000,0.500), Y(-0.500,0.000,0.000), S(-0.500,0.500,0.000), X(0.000,0.500,0.000), U(0.000,0.500,0.500) and R(-0.500,0.500,0.500)
<b>Position of the Fermi level</b>	Near valence band
<b>Dispersion in top of the Valence Bands (VBs) and in bottom of the Conduction Band (CBs)</b>	<b>Top of VBs:</b> 53.53 meV <b>Bottom of CBs:</b> 52.57 meV
<b>Position of the lowest conduction band minima (CBM) and corresponding energy</b>	$\Gamma$ k-point $E_{CBM} = 2.835$ eV
<b>Position of the highest valence band maxima (VBM) and corresponding energy</b>	$Z$ k-point $E_{VBM} = 0.000$ eV
<b>Value and the nature of the theoretical band gap</b>	Indirect band gap, $E_g = 2.835$ eV
<b>Experimental value of bandgap from UV-DRS plot</b>	3.179 eV
<b>Comparison of bandgaps as calculated with GGA/PBE solid</b>	$E_g^{Cal} < E_g^{Expt}$
<b>Nature of the material</b>	<b>p-type wide bandgap semiconductor</b>

### Hirshfeld surface analysis and Fingerprint Plots: Details of colour code used:

The Hirshfeld surface analysis can provide details description of noncovalent interactions by displaying all the intermolecular interactions and the two-dimensional fingerprint plot quantifies these interactions within the crystal structure. The normalized contact distances,  $d_{norm}$ , based on vander Waals radii, are mapped into the Hirshfeld surfaces to compare the intermolecular interactions within the crystal structure. In the colour scale, negative values of  $d_{norm}$  are visualized by the red colour, indicating contacts shorter than the sum of vander Waals radii. The white colour denotes intermolecular distances close to vander Waals

contacts with  $d_{\text{norm}}$  equal to zero. Consequently, contacts longer than the sum of vander Waals radii with positive  $d_{\text{norm}}$  values are indicated by blue colour. The short O...H/H...O contacts in the molecules can be seen in Hirshfeld surface as red bright spots and other weaker and longer contacts are observed as light red spots. Shape index is the measurement of “which shape” and it is sensitive to very fine changes in the shape of the surface where the total curvature is very low. The curvedness is the measurement of “how much shape” of the surface. The flat areas of the surface have low values of curvedness while sharp curvature areas correspond to high values of curvedness and usually tend to divide the surface into patches, indicating interactions between neighbouring molecules. The 2D fingerprint plots which examine all of the intermolecular contacts at the same time, reveal that the main intermolecular interactions in the molecules are O...H/H...O, H...Br, Br...C, C...H, Br...O intermolecular interactions.

**Molecular Electrostatic Surface Potential:** The location and nature of the electrophilic and nucleophilic regions of the individual components of the co-crystal and four above mentioned self-assembled interacting dimeric forms within the crystal lattice along with their role in generating noncovalent interactions have been probed by computing the molecular electrostatic surface potential (MESP) from the distribution of electron density as calculated over their optimized geometries. The molecular electrostatic potential (MEP) isosurfaces have been represented in Figure S24. The electronegative regions i.e., sites with low electrostatic potential (negative MEP values) are situated near N-atoms (QUIN) and at O-atoms (not participating in hydrogen bonding) (TBTA), whereas electropositive regions related to high electrostatic potential (positive MEP values) are located near the H-atom of C–H (QUIN) and O–H (TBTA) groups. Again, the MEP value over the six membered aromatic ring of TBTA is more positive ( $\pi$ -hole) than that over the QUIN ring (electron rich), providing adequate electrophilic and nucleophilic regions for extended H-bonding interaction or  $\pi$ -acidity/basicity for establishing  $\pi$ -stacking interactions ( $\pi\text{h}\cdots\pi$ ) between these two electron rich and electron deficient aromatic surfaces. The XB interactions between sigma hole of Br atom and electron-rich surface of O atom form the Br...O short contact. In each type of self-assembled dimer, regions with both the negative and positive MEP values, suitable for interacting with electrophilic or nucleophilic regions of other species, are found.

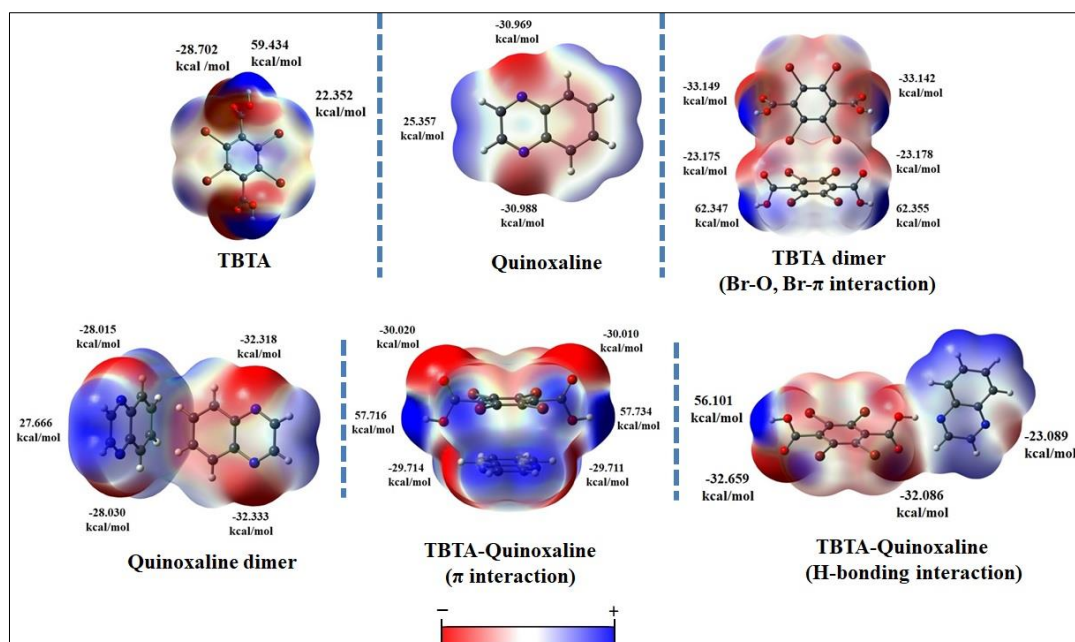


**Figure S24.** Molecular electrostatic potential (MEP) surface mapped onto electron density isosurface of value 0.001 au where, the electropositive, electronegative and the neutral isosurface regions are indicated by blue, red and white colours respectively.

**Change in absorption behaviour of the co-crystal from its coformer:** Absorption spectra of the co-crystal show two different bands (Figure S16). We have simulated the UV-vis absorption spectra of the co-crystal in aqueous phase and the results of which has been provided in Table S12-S13. The lower energy band has a peak at 322 nm which is similar to the absorption spectra of individual QUIN moiety. The high energy band consists of two distinct peaks. The first peak is at 225 nm (its nearby theoretical peak is located at 224 nm) corresponds to TBTA, which has a peak at 222 nm and another peak at 235 nm (its nearby theoretical peaks are located at 233 nm and 249 nm) corresponds to QUIN, which has a peak at 234 nm. A small hump is observed at 230 nm (its nearby theoretical peaks are located at 230 nm and 232 nm). There is no trace of any peak for the individual coformers (TBTA and QUIN) in the surrounding of this small hump. Thus it can be attributed to the presence of supramolecular assembly of TBTA and QUIN in solution phase. Charge transfer (CT) band which is usually observed at substantially higher wavelength compared to bands of the components. However, no such CT band has been observed in the aqueous phase UV-vis spectrum of the sample.



### Photoconductivity in the light of thermionic emission (TE) theory:

For further investigation of the fabricated devices, we have analyzed the IV curve (Figure S25) using the thermionic emission theory for Region I and determined different parameters of the device while in Region II, the SCLC theory has been employed to estimate the charge transport parameters of the device.

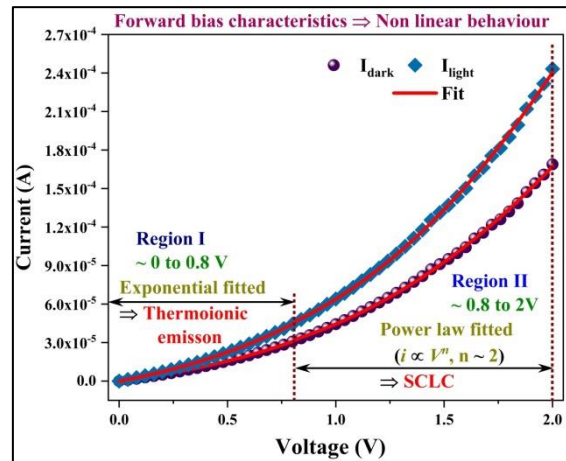


**Figure S25:** Identification of Thermionic emission region (Region I) and space charge limited current region (Region II) within the I-V characteristics under the application of forward bias.

For the Region I we have employed the thermionic emission (TE) theory. The current voltage (I-V) relationship of a schottky diode can be written as<sup>31</sup>

$$I = I_0 \left[ \exp\left(\frac{qV}{\eta kT}\right) - 1 \right] \quad (1)$$

Here, I stands for the forward current at bias voltage V at temperature T (in Kelvin).  $\eta$  is the ideality factor of the device, q is the charge of an electron and k is the Boltzmann constant.  $I_0$  can be expressed as<sup>31</sup>

$$I_0 = AA^*T^2 \exp\left(\frac{-q\phi_b}{kT}\right) \quad (2)$$

Where A,  $A^*$  and  $\phi_b$  are the effective area of the diode, Richardson constant of the synthesized material and the barrier height of the device respectively. The value of the ideality factor ( $\eta$ ), series resistance ( $R_s$ ) and the barrier height ( $\phi_b$ ) of Al/synthesized sample/ITO are measured from the following equations<sup>32</sup>

$$\frac{dV}{d\ln(I)} = \frac{\eta kT}{q} + IR_s \quad (3)$$

$$H(I) = V - \left(\frac{\eta kT}{q}\right) \ln\left(\frac{I}{AA^*T^2}\right) \quad (4)$$

This equation (4) can be rewritten as

$$H(I) = IR_S + \eta\phi_b \quad (5)$$

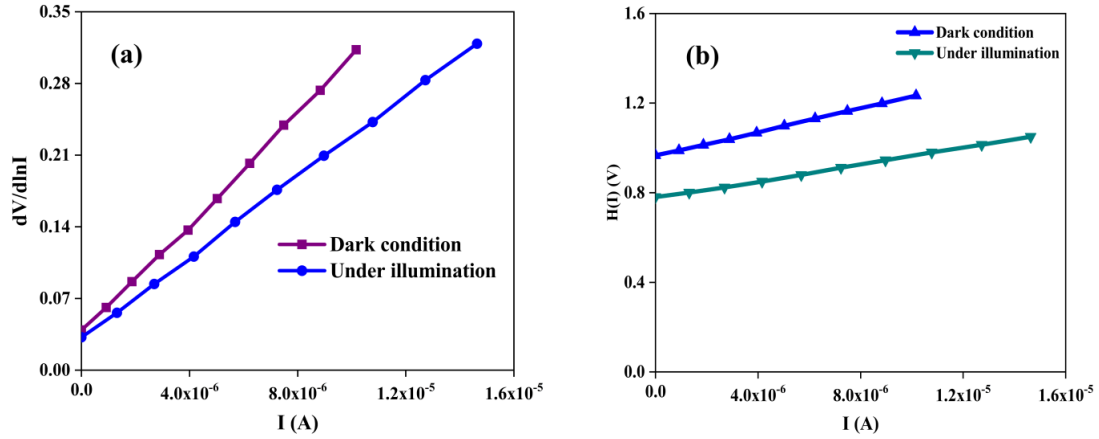


**Figure S26:** (a)  $dv/d\ln I$  versus  $I$  plot and (b)  $H(I)$  versus  $I$  plot of the SBDs under dark and light condition respectively.

The  $dv/d\ln I$  versus  $I$  graph for the SBD under dark and light condition are portrayed in the Figure S26 (a). The value of the ideality factor and the series resistance is determined from the y-axis intercept and the slope of the  $dv/d\ln I$  versus  $I$  plot (Figure S26 (a)) respectively. Figure S26 (b) represents the  $H(I)$  versus  $I$  curve of the diodes under dark and light condition respectively. This graph is linear and the y-axis intercept of these representations give the schottky barrier height of the device. We can also find the series resistance from the slope of the  $H(I)$  versus  $I$  curve which is the other way to determine the value of  $R_s$ . All the obtained values of electrical parameters are listed in Table S15. It can be observed that the values of ideality factors are deviated from the ideal value of unity. This deviation indicates the presence of the series resistance, existence of the interface states and the barrier inhomogeneities.<sup>33-34</sup> Under illumination, the value of ideality factors for the diode approached towards unity. We have seen that value of series resistance measured from the  $dv/d\ln I$  versus  $I$  and  $H(I)$  versus  $I$  curve are more or less same. The barrier heights of the Al/cocrystal/ITO are estimated to be 0.70 eV and 0.65 eV under dark and light condition respectively (Table S15).

**Table S15:** Important electrical parameters of the Al/cocrystal/ITO device.

SBD based on	Condition	On/off	S	Conductivity $\times 10^{-5}$ (S cm <sup>-1</sup> )	$\eta$	$R_s$ (K $\Omega$ )		$\Phi_b$ (eV)
						$dv/d\ln I$ vs. I	$H(I)$ vs. I	
Co-crystal	Dark	41	0.45	0.56	1.36	26.97	26.50	0.70
	Light	56		0.76	1.19	19.72	18.77	0.65

For further analysis of charge transport behaviour of Al/cocrystal junctions, we have plotted the I-V curve (Figure S27 (a)) in log-log scale. In the forward bias voltage region, the current voltage relation can be written as  $I \propto V^m$ , where  $m$  is the slope of this plot (Figure S27 (a)). It is seen that the Figure S27 (a) consists of two different regions with different values of  $m$ . In the lower bias region (Region 1), the value of slope is measured as close to unity. In Region 2, the value of  $m$  is very close to 2, the current voltage characteristics of the junctions can be expressed as,  $I \propto V^2$ . This particular region (Region 2) is referred as the space charge limited current (SCLC) regime. We have introduced the standard SCLC theory to estimate the charge transport parameters such as effective charge carrier mobility ( $\mu_{eff}$ ), transit time ( $\tau$ ) and charge carrier concentration ( $N$ ) of the SBDs.

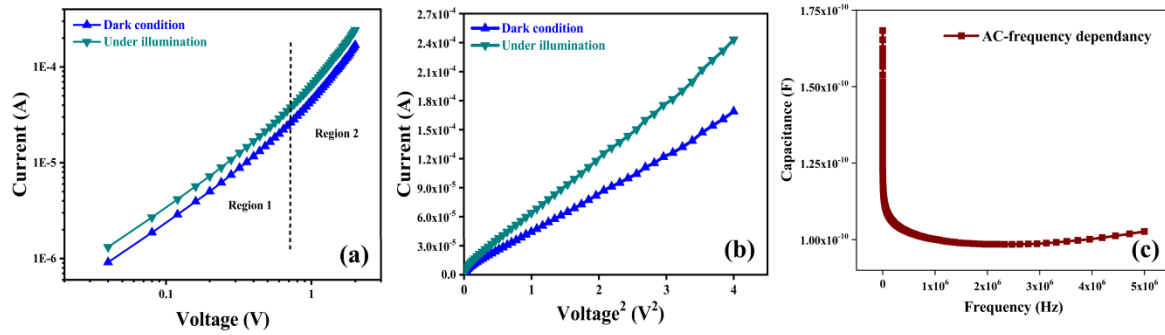


**Figure S27:** (a) Current-voltage (I-V) characteristics (in log-log scale), (b) Current versus voltage<sup>2</sup> (I versus V<sup>2</sup>) plot and (c) capacitance versus frequency (C versus F) of the cocrystal based SBDs.

The effective charge carrier mobility ( $\mu_{eff}$ ) is calculated in the SCLC region from the slope of the I versus V<sup>2</sup> plot (Figure S27 (b)) with the help of the following Mott-Gurney equation<sup>32,35</sup>

$$I = \frac{9\mu_{eff} \epsilon_0 \epsilon_r A}{8} \left( \frac{V^2}{d^3} \right) \quad (6)$$

Where,  $d$  is the thickness of the active thin film,  $A$  is the effective diode area and  $\epsilon_0$  is the permittivity of free space. Here  $\epsilon_r$  is referred as the dielectric constant and it can be estimated from the following equation

$$\epsilon_r = \frac{1}{\epsilon_0} \cdot \frac{C \cdot d}{A}$$

where  $C$  is the capacitance at higher frequency (Figure S27 (c)). The calculated values of  $\epsilon_r$  for cocrystal are 1.60. The transit time ( $\tau$ ) of the charge carriers is obtained using the equation<sup>30</sup>

$$\tau = \frac{9\varepsilon_0\varepsilon_r A}{8d} \left(\frac{V}{I}\right) \quad (7)$$

The another crucial parameter is charge carrier concentration (N) and it can be estimated by introducing the equation<sup>31</sup>

$$N = \frac{\sigma}{q\mu_{\text{eff}}} \quad (8)$$

The estimated values of the charge carrier mobility ( $\mu_{\text{eff}}$ ), transit time ( $\tau$ ) and charge carrier concentration (N) are presented in Table S16.

**Table S16:** Charge transport parameter of the co-crystal based SBD

Device based on	Condition	$\mu_{\text{eff}} \times 10^{-7}$ ( $\text{m}^2 \cdot \text{V}^{-1} \cdot \text{S}^{-1}$ )	$\tau \times 10^{-7}$ (S)	$\mu_{\text{eff}} \tau \times 10^{-13}$ ( $\text{m}^2 \cdot \text{v}^{-1}$ )	$N_D \times 10^{20}$ ( $\text{eV} \cdot \text{m}^{-3}$ )
Cocrystal	Dark	4.44	3.9	1.73	3.57
	Light	6.86	2.7	1.87	3.79

So according to Thermionic emission theory, the co-crystal shows photo-responsive Schottky barrier diode behavior and barrier height of conductivity decreases under UV-irradiation.

#### Calculation of energy level of the components and the dimer geometries:

The analysis of the HOMO, LUMO energy levels of the individual components on the ground state geometries show that HOMO-LUMO levels of TBTA and QUIN lie at almost same energies. (Figure S28 and Table S17).

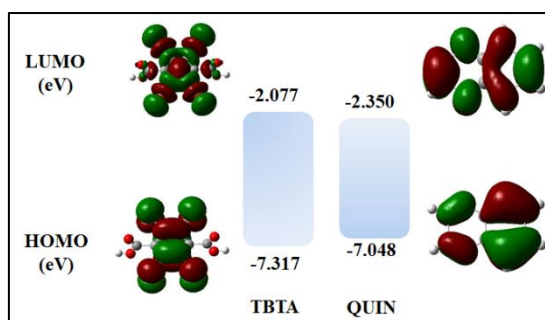


**Figure S28:** Molecular orbitals of the components at B3LYP-GD3BJ/6-311++G(d,p) level.

However, after formation of the co-crystal through self-assembly, the components can no longer be treated as separate and isolated entities maintaining their individual characteristics rather they interact with each other due to close proximity. The interactions between the components within the co-crystal change the electron charge distribution of the

individual isolated components. In consequence the M.O. energy levels and electronic band structure should be different compared to their individual isolated cofomers.

**Table S17:** HOMO-LUMO energy levels (in eV) of the components TBTA and QUIN and their hydrogen bonded dimer calculated with various functional and basis sets.

Functional & Basis set	TBTA		QUINOXALINE		H-bonded dimer	
	LUMO	HOMO	LUMO	HOMO	LUMO	HOMO
B3LYP-GD3BJ/6-311++G(d,p)	-2.07732	-7.31742	-2.35025	-7.0483	-2.88005	-7.08013
B3LYP-GD3BJ/6-31G+(d,p)/LANL2DZ	-2.25174	-7.40449	-2.29827	-6.98816	-2.8708	-7.15197
M06-2X/6-31G+(d,p)	-1.07213	-8.52969	-1.29771	-8.27335	-1.84684	-8.40587
M06-2X/6-31G+(d,p)/LANL2DZ	-1.15104	-8.64044	-1.29771	-8.27335	-1.8316	-8.29567

#### References:

1. *SHELXS 97, Program for Structure Solution*, Sheldrick, G. M. University of Göttingen, Germany, **1997**.
2. *SHELXL 97, Program for Crystal Structure Refinement*, Sheldrick, G. M. University of Göttingen, Germany, **1997**.
3. Spek, A. L. Single-crystal structure validation with the program PLATON. *J. Appl. Crystallogr.*, **2003**, *36*, 7–13.
4. Farrugia, L. J. ORTEP-3 for Windows - a version of ORTEP-III with a Graphical User Interface (GUI). *J. Appl. Crystallogr.*, **1997**, *30*, 565.
5. Farrugia, L. J. WinGX suite for small-molecule single-crystal crystallography. *J. Appl. Crystallogr.*, **1999**, *32*, 837–838.
6. *Gaussian 09, Revision A.02*, Frisch, M. J.; Trucks, G. W.; H. B. Schlegel, G. E. Scuseria, M. A. Robb, J. R. Cheeseman, G. Scalmani, V. Barone, G. A. Petersson, H. Nakatsuji, X. Li, M. Caricato, A. V. Marenich, J. Bloino, B. G. Janesko, R. Gomperts, B. Mennucci, H. P. Hratchian, J. V. Ortiz, A. F. Izmaylov, J. L. Sonnenberg, D. Williams-Young, F. Ding, F. Lipparini, F. Egidi, J. Goings, B. Peng, A. Petrone, T.

- Henderson, D. Ranasinghe, V. G. Zakrzewski, J. Gao, N. Rega, G. Zheng, W. Liang, M. Hada, M. Ehara, K. Toyota, R. Fukuda, J. Hasegawa, M. Ishida, T. Nakajima, Y. Honda, O. Kitao, H. Nakai, T. Vreven, K. Throssell, J. A. Montgomery, Jr., J. E. Peralta, F. Ogliaro, M. J. Bearpark, J. J. Heyd, E. N. Brothers, K. N. Kudin, V. N. Staroverov, T. A. Keith, R. Kobayashi, J. Normand, K. Raghavachari, A. P. Rendell, J. C. Burant, S. S. Iyengar, J. Tomasi, M. Cossi, J. M. Millam, M. Klene, C. Adamo, R. Cammi, J. W. Ochterski, R. L. Martin, K. Morokuma, O. Farkas, J. B. Foresman, and D. J. Fox, Gaussian, Inc., Wallingford CT, **2016**.
7. Becke, A. D. Density-functional thermochemistry. III. The role of exact exchange. *J. Chem. Phys.*, **1993**, *98*, 5648-5652.
  8. Lee, C. T.; Yang, W. T. and Parr, R. G., Development of the Colle-Salvetti correlation-energy formula into a functional of the electron density. *Phys. Rev. B.*, **1988**, *37*, 785-789.
  9. Hay, P. J. and Wadt, W. R, Ab initio effective core potentials for molecular calculations - potentials for K to Au including the outermost core orbitals, *J. Chem. Phys.*, **1985**, *82*, 299-310.
  10. Grimme, S.; Ehrlich, S.; Goerigk, S. L. Effect of the damping function in dispersion corrected density functional theory. *J. Comput. Chem.*, **2011**, *32*, 1456–1465.
  11. Boys, S. F. and Bernardi, F. Calculation of Small Molecular Interactions by Differences of Separate Total Energies - Some Procedures with Reduced Errors, *Mol. Phys.*, **1970**, *19*, 553-566.
  12. Lu, T.; Chen, F. Multiwfn: A Multifunctional WavefunctionAnalyzer, *J. Comput. Chem.*, **2012**, *33*, 580-592.
  13. Humphrey, W.; Dalke, A. and Schulten, K. VMD - Visual Molecular Dynamics, *J. Molec. Graphics*, **1996**, *14.1*, 33-38.
  14. Turner, M. J.; Mckinnon, J. J.; Wolff, S. K.; Grimwood, D. J.; Spackman, P. R.; Jayatilaka, D. and Spackman, M. A. **2017**, Crystal Explorer 17, The University of Western Australia.
  15. Turner, M. J.; Grabowsky, S.; Jayatilaka, D. and Spackman, M. A. Accurate and Efficient Model Energies for Exploring Intermolecular Interactions in Molecular Crystals, *J Phys Chem Lett.*, **2014**, *5*, 4249-4255.

16. Tan, S. L.; Jotani, M. M. and Tiekink, E. R. T. Utilizing Hirshfeld surface calculations, non-covalent interaction (NCI) plots and the calculation of interaction energies in the analysis of molecular packing, *Acta Cryst.*, **2019**, *E75*, 308–318.
17. Mackenzie, C. F.; Spackman, P. R.; Jayatilaka, D.; and Spackman, M. A. CrystalExplorer model energies and energy frameworks: extension to metal coordination compounds, organic salts, solvates and open-shell systems, *IUCrJ*, **2017**, *4*, 575–587.
18. Saini, Y.; Mahajan, S.; Kapoor, K. K.; Hundal, G. and Seth, S.K. Diverse structural assemblies of a series of ninhydrin derivatives: Quantitative analyses from experimental and theoretical studies, *J. Mol. Struct.*, **2020**, *1224*, 128920-128932.
19. O'Boyle, N. M.; Tenderholt, A. L.; Langner, K. M. cclib: a library for package-independent computational chemistry algorithms. *J. Comp. Chem.*, **2008**, *29*, 839-845.
20. Roy, S.; Pramanik, S.; Ghorui, T.; Pramanik, K. Insight into luminescent bisazoaromatic CNN pincer palladacycle: synthesis, structure, electrochemistry and some catalytic applications in C–C coupling. *RSC Adv.*, **2015**, *5*, 22544-22569.
21. Roy, L. E.; Scalmani, G.; Kobayashi, R.; Batista, E. R. Theoretical Studies on the Stability of Molecular Platinum Catalysts for Hydrogen Production. *Dalton Trans.*, **2009**, *0*, 6719-6721.
22. Das, U.; Ghorui, T.; Adhikari, B.; Roy, S.; Pramanik, S.; Pramanik, K. Iridium-mediated C–S bond activation and transformation: organoiridium(III) thioether, thiolato, sulfinato and thiyl radical compounds. Synthesis, mechanistic, spectral, electrochemical and theoretical aspects. *Dalton Trans.*, **2015**, *44*, 8625-8639.
23. Chopra, S. Excited state analysis of absorption processes in metal decorated graphene nanoribbons. *RSC Adv.*, **2016**, *6*, 20565–20570.
24. Clark, S. J.; Segall, M. D.; Pickard, C. J.; Hasnip, P. J.; Probert, M. J.; Refson, K.; Payne, M. C. First principles method using CASTEP. *Z. Kristallogr.*, **2005**, *220*, 567–570.
25. Perdew, J. P.; Burke, K.; Ernzerhof, M. Generalized gradient approximation made simple. *Phys. Rev. Lett.*, **1996**, *77*, 3865–3868.
26. Vanderbilt, D. Soft self-consistent pseudopotentials in a generalized eigenvalue formalism. *Phys. Rev. B.*, **1990**, *41*, 7892–7895.
27. Monkhorst, H. J.; Pack, J. D. Special points for Brillouin-zone integrations. *Phys. Rev. B.*, **1976**, *13*, 5188-5192.

28. Grimme, S. Semiempirical GGA-type density functional constructed with a long-range dispersion correction. *J. Comput. Chem.*, **2006**, *27*, 1787-1799.
29. Ephraim Babu, K.; Veeraiah, A.; TirupatiSwamy, D. and Veeraiah, V. First-Principles Study of Electronic Structure and Optical Properties of Cubic Perovskite CsCaF<sub>3</sub>. *CHIN. PHYS. LETT.*, **2012**, *29*, 117102.
30. Yang, L. -M.; Ganz, E.; Svellec S. and Tilset, M. Computational exploration of newly synthesized zirconium metal–organic frameworks UiO-66, -67, -68 and analogues. *J. Mater. Chem. C*, **2014**, *2*, 7111–7125.
31. Cheung, S. K. and Cheung N. W. Extraction of Schottky diode parameters from forward current-voltage characteristics. *Appl. Phys. Lett.*, **1986**, *49*, 85-87.
32. Dey, A.; Layek, A.; Roychowdhury, A.; Das, M.; Datta, J.; Middy, S.; Das, D. and Ray, P. P. Investigation of charge transport properties in less defective nanostructured ZnO based Schottky diode. *RSC Adv.*, **2015**, *5*, 36560–36567.
33. Gupta, R. K. and Yakuphanoglu, F. Photoconductive Schottky diode based on Al/p-Si/SnS<sub>2</sub>/Ag for optical sensor applications. *Sol. Energy*, **2012**, *86*, 1539–1545.
34. Das, M.; Datta, J.; Dey, A.; Jana, R. Layek, A.; Middy, S. and Ray, P. P. One step hydrothermal synthesis of arGO–TiO<sub>2</sub> nanocomposite and its application on a Schottky diode: improvement in device performance and transport properties. *RSC Adv.*, **2015**, *5*, 101582-101592.
35. Das, M.; Datta, J.; Jana, R. Sil, S.; Halder, S. and Ray, P. P. Synthesis of rGO–Zn<sub>0.8</sub>Cd<sub>0.2</sub>S via in situ reduction of GO for the realization of a Schottky diode with low barrier height and highly enhanced photoresponsivity. *New J. Chem.*, **2017**, *41*, 5476-5486.